The simulation of transport processes in cementitious materials with embedded healing systems

Brubeck Lee Freeman, Tony Jefferson

Abstract

A new model for simulating the transport of healing agents in self-healing (SH) cementitious materials is presented. The model is applicable to autonomic SH material systems in which embedded channels, or vascular networks, are used to supply healing agents to damaged zones. The essential numerical components of the model are a crack flow model, based on the Navier-Stokes equations, which is coupled to the mass balance equation for simulating unsaturated matrix flow. The driving forces for the crack flow are the capillary meniscus force and the force derived from an external (or internal) pressure applied to the liquid healing agent. The crack flow model component applies to non-uniform cracks and allows for the dynamic variation of the meniscus contact angle, as well as accounting for inertial terms. Particular attention is paid to the effects of curing on the flow characteristics. In this regard, a kinetic reaction model is presented for simulating the curing of the healing agent and a set of relationships established for representing the variation of rheological properties with the degree of cure. Data obtained in a linked experimental programme of work is employed to justify the choice and form of the constitutive relationships, as well as to calibrate the model's evolution functions. Finally, a series of validation examples are presented that include the analysis of a series of concrete beam specimens with an embedded vascular network. These examples demonstrate the ability of the model to capture the transport behaviour of this type of SH cementitious material system.

Keywords

Transport model, Finite element, Self-healing, Coupled models, Multi-physics

1 Introduction

Despite being one of the most widely used materials in construction, concrete frequently suffers from significant durability problems, which are usually associated with cracking. These problems include alkali-silica reaction, reinforcement corrosion and calcium leaching,[1-3] all of which contribute to the high maintenance and repair costs associated with concrete structures.[4] One approach to mitigating this problem is to design the concrete to be self-healing (SH), such that cracks heal as they form. A wide range of approaches have been employed for achieving this; some of these are classified as 'autonomic' (or manufactured) healing techniques, whilst other methods enhance the natural 'autogenous' healing capabilities of cementitious materials.[5] A significant number of these SH technologies utilise encapsulated healing agents that are released and transported to damage sites when cracking occurs.[6] The techniques differ in the methods used for encapsulation, release and delivery, as well as in the type of healing agent used. Methods of embedding healing agents within the cementitious matrix include microencapsulation,[7,8] macro-encapsulation,[9,10] and vascular networks.[11,12] Healing agents range from bacterial spores,[13,14] to mineral admixtures,[7,9] and adhesives.[11,15] Full reviews of self-healing technologies and associated experimental characterisation techniques can be found in De Belie et al.,[6] Ferrara et al.,[16] Sidiq et al.,[17] and Xue et al.[18]

There is now an ever expanding body of work on numerical modelling of SH systems, with significant progress having been made in recent years.[19-27] A number of these authors have acknowledged the complexity of SH systems and have highlighted the many interacting physical processes that govern the behaviour of these systems. To date, few models fully consider the coupling between the transport, curing and mechanical healing processes of SH systems.[27] In addition, the validation of many previous models against experimental data has been limited. A comprehensive review of numerical models for SH systems can be found in Jefferson et al.,[27] with exception of the most recent of contributions (see for example, Algaifi et al.,[28] Mauludin et al.,[29] Oucif et al.,[30,31] Ponnusami et al.,[32] Shahsavari et al.,[33] Voyiadjis and Kattan,[34] Zhang and Zhuang,[35] and Sanz-

Herrera et al.[36]). Here, only recent relevant papers that address transport processes in SH materials are considered in more detail.

Algaifi et al.[28] developed a model for SH bio-concrete that simulates the microbial precipitation of calcium carbonate. Urea transport, urea hydrolysis (including the effect of bacterial cell concentration) and calcite production were all taken into account in the model formulation. The transport of urea was simulated using Fick's law, whilst the reactions were modelled using first order kinetics. To verify the predicted crack healing, experimental work was carried out on a self-healing beam. The model results compared well with the experimental data, with the former predicting complete healing in 60 days, which compared with 70 days from the measured data.

Sanz-Herrera et al.[36] presented a coupled mechano-chemical-diffusive model for SH materials. Their model couples a continuum damage mechanics (CDM) model with a reactive diffusive chemical model. The CDM model was developed under the strain equivalence hypothesis and used a rate-dependent damage evolution model derived from that presented by Darabi et al.[37] The chemical diffusive model was based on a self-healing mechanism in which a mobile species is transported into the material from the environment and reacts with a static species present in the matrix material. The diffusion of the mobile species was modelled using Fick's law, whilst the reaction was modelled using first order kinetics. The performance of the model was demonstrated through a series of numerical experiments concerning the cyclic loading of self-healing materials.

Many numerical transport models for cementitious materials have concentrated on moisture and ion transport associated with carbonation and autogenous healing.[22,38-42] Although such models have general relevance to this study, it is previous work on simulating the flow of autonomic healing agents in discrete cracks, and the associated continuum matrix flow, that has greater importance for the present work.[43-46] Gardner et al.'s model used a modified Lucas-Washburn equation that allowed for stick-slip of the meniscus, frictional dissipation and wall slip, to simulate liquid flow in discrete cracks.[43-45] The model was shown to be able to accurately predict the capillary rise response of a range of healing agents in both natural and artificial cracks. Gilabert et al.[46] used the open source computational fluid dynamics code OpenFOAM,[47] to simulate the flow of a healing agent in artificial concrete cracks for a range of crack openings. Their model used the Navier-Stokes equations to simulate flow in the embedded healing-agent supply tubes and within the crack plane. The authors introduced a piecewise linear contact-angle v time relationship, which was constructed from their own experimental data. The simulations were in reasonable agreement with their experimental observations. With the exception of the work of Gardner et al.[43-45] and Gilabert et al.,[46] there has been little (or no) other work on simulating the flow of autonomic healing agents in discrete cracks in SH cementitious materials. However, there is a large body of work on modelling coupled matrix and crack (or capillary) flow processes for other applications. Such models have been used for assessing the performance of nuclear waste repositories,[48] predicting hydraulic fracture simulation in the oil and gas industry,[49] studying moisture effects on the mechanical behaviour of building materials,[50-52] and predicting blood flow and drug delivery in tumours.[53,54]

The above paper by Lecampion et al.[49] reviews recent work on modelling hydraulic fracture. In general, the fracture fluid flow in such models is based on mass and momentum balance equations, with the inertial terms usually being neglected. Carter's leak-off model is often used to calculate the loss of fluid to the surrounding medium.[55] Carter's model uses a 1D diffusion equation to give the leak off-rate, based on the assumptions that the rate of matrix diffusion is small compared to the fracture propagation rate, and that the net fluid pressure is much smaller than the far-field effective stress. A number of models couple continuum flow to the fracture flow to avoid the assumptions of Carter's model,[56,57] whilst others take into consideration the non-Newtonian behaviour of the fracturing fluid, including shear rate dependency and the effects of proppants suspended in the fluid.[58,59] In hydraulic fracture, fluid flow and mechanical behaviour are strongly coupled processes. The dynamic fracturing was investigated by Cao et al.[57] (see also Milanese et al.[60]), whose

model was able to capture the step-wise crack advancement and corresponding fluid pressure oscillations observed in a number of experiments (e.g. Pizzocolo et al.[61]).

Soltani and Chen,[53] presented a coupled model of interstitial fluid and blood flow through a tumour. Their model allows for a network of interconnected capillaries and takes into account the non-Newtonian behaviour of blood, as well as the blood phase separation at bifurcations. The blood flow in the capillaries was calculated using Poiseuille's law, whilst the tumour tissue was treated as a saturated porous medium, with Darcy's law being used to describe the flow. The two were coupled through the transvascular flow rate, which is given as a function of the difference in pressure between the blood and the interstitial fluid through Starling's law. The predictions of the model were shown to compare well with experimental data. It is interesting to compare blood flow models, such as that presented by Soltani and Chen[53], with models for fluid flow in fractured porous media. Both sets of models consider fluid flow in capillary networks (i.e. blood vessels in the former case and crack networks in the latter) coupled to continuum flow in a porous medium (e.g. surrounding tissue and concrete matrix respectively), and both are based on the same basic mass balance and fluid flow equations. The differences between the two sets of models results from the contrasting physical, chemical and biological processes of the respective systems, which necessitate very different constitutive models for the fluid and mechanical systems, as well as different equations for coupling fluid transport to the solid-mechanics component of the models. For example, blood is normally simulated as a non-Newtonian fluid -with an associated constitutive relationship- whereas the fluids modelled in fracturing media are normally assumed to be Newtonian in nature. In blood flow systems, there is strong coupling between the large deformations of the biological tissue and the fluid flow behaviour, whereas in many fractured porous media applications (e.g. flow in building materials) the porous media is much stiffer than the fluid and the evolving network of cracks is the dominate feature of the mechanical system.

A model for the moisture uptake of cracked building materials has been presented by Roels et al.[50] (see also Roels et al.[51] and Carmeliet et al.[52]). The model considered unsaturated moisture flow in the continuum, governed by the moisture mass balance equation, with Darcy's law being used to describe the moisture flux. This was coupled to the flow in the discrete crack through a source/sink term, representing flow through the crack faces. Discrete crack flow was modelled using Poiseuille's law and a quasi-static pressure equation, which were solved in a staggered solution algorithm. The accuracy of the model was demonstrated through a series of validation tests, which considered the preferential uptake of moisture in naturally and artificially cracked bricks.

de Borst and co-workers developed a set of sub-grid scale models for fluid flow in fractured and fracturing porous media.[56,62,63] The models consider both saturated and unsaturated flow, coupled to the deformation of the solid phase through the linear momentum balance equation. For the crack flow, both flow in fully open cracks and flow in partially open cracks were considered. For the former, the flow was governed by Stokes equations, whilst for the latter, the crack was treated as a porous medium, but with a much higher permeability than the surrounding continuum. The crack flow was coupled to the matrix flow through a mass coupling term, which represents a fluid flux discontinuity across the crack. In de Borst,[56] the fluid pressure distribution across a crack is discussed in detail and a set of interface element formulations are presented that address the following cases; pressure continuity, pressure discontinuity and an independent pressure in the crack. A particular feature of the models is that they are applicable to a range of different discretisations, including isogeometric interface elements, which allow for a higher order continuity of the pressure and displacement fields. The performance of the model was demonstrated through a range of example calculations.

An aspect of capillary flow behaviour that was not taken into account in many of the aforementioned models was the variation with velocity of the angle of contact between a fluid meniscus and the substrate. This dynamic contact angle (DCA) variation can have a significant effect on the flow in a crack,[64] particularly when a vascular SH system employs a pressurised flow network for healing agent delivery. Another aspect of behaviour that has not been addressed in previous SH transport models is the effect of curing on the flow

properties of fluid healing agents. Both of these issues are considered explicitly in the present model formulation.

The aim of the work described in this paper is to develop a comprehensive coupled model to simulate the transport processes in cementitious SH systems with embedded healing agents. The work focused on SH systems that use single-component adhesives as a healing agent, but could readily be extended to multi-component agents, through the addition of a second phase.

The innovations of this work are;
  (i)   a new model for flow in discrete cracks that considers fluid inertia, the dynamic variation in the meniscus contact angle, healing agent curing and rheology changes, tapering cracks and the coupled unsaturated flow in the surrounding matrix;
  (ii)   a new approach for simulating the kinetic curing of a single-agent adhesive, based on new experimental observations;
  (iii)   calibration of the model components using experimental data from others, as well as new data obtained by the authors' group in Cardiff;
  (iv)   validation of the model using new experimental data.

The layout of the remainder of this paper is as follows;
  - Section 2 presents the theoretical formulation of the model;
  - Section 3 presents the numerical solution;
  - Section 4 presents the dynamic contact angle theory and calibration;
  - Section 5 presents the healing agent curing model, the rheological model, a wall-slip model and calibrations;
  - Section 6 presents a series of validation examples concerning the flow of cyanoacrylate (CA) through concrete specimens;
  - Section 7 presents the discussion.
  - Section 8 presents some conclusions.

2 Theoretical Formulation

The problem domain is defined as $\Omega \in \mathbb{R}^d$ with boundary Γ. The domain is made up of subdomains representing the discrete macro cracks (which may cross the underlying continuum mesh arbitrarily) and the continuum concrete matrix, denoted Ω_{crk} and Ω_{mtx} respectively, such that $\Omega = \Omega_{crk} \cup \Omega_{mtx}$ and where $\Omega_{crk} \in \mathbb{R}^1$ and $\Omega_{mtx} \in \mathbb{R}^2$. The boundaries of the subdomains are similarly defined as Γ_{crk} and Γ_{mtx}, such that $\Gamma = \Gamma_{crk} \cup \Gamma_{mtx}$. The time period considered is $t \in [t_0, T]$.

Damage-healing behaviour

The mechanical damage-healing behaviour is the subject of a forthcoming paper by the authors, and so here only a brief outline is presented of this component of the work. A cohesive zone model is used for the mechanical behaviour of the concrete (See Appendix) which uses elements with embedded strong discontinuities (SD).[65] Crack path continuity is ensured using an algorithm based on that found in Alfaiate et al.[66,67] The model allows for simultaneous damage-healing, re-damage of healed material and multiple healing cycles.

Discrete crack flow

Assuming that the air pressure within the crack remains constant at atmospheric pressure,[52] and that the viscous stresses in the air are negligible, the governing equations for the discrete crack flow are the 1D incompressible single fluid Navier-Stokes equations.[68-70] The governing momentum balance equation is given as:

$$\frac{\partial(\rho_h u)}{\partial t} + u\frac{\partial(\rho_h u)}{\partial \chi} = -\frac{\partial P_{hcrk}}{\partial \chi} + \rho_h g sin\phi + f - \rho_h u Q_{crk} \quad \forall\, \mathbf{x} \in \Omega_{crk} \qquad (1)$$

where u is the cross-section averaged healing agent flow velocity, χ is a convected coordinate (See Figure 1), ρ_h is the healing agent density, $\partial P_{hcrk}/\partial \chi$ is the pressure gradient, g is the acceleration due to gravity, ϕ is the inclination of the crack, f is a viscous resistance term and Q_{crk} is a source/sink term for flow between the crack and the matrix, as illustrated in Figure 1.
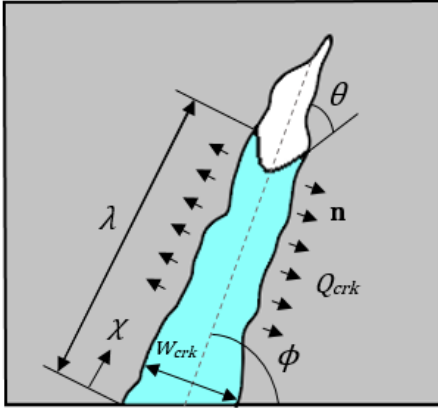

Figure 1 – Schematic depicting flow in a discrete crack (where dependencies have been dropped for clarity)

Assuming Poiseuille flow conditions,[43-45,69,70] and adding a factor to allow for wall slip,[43,44,71] the viscous resistance term is given by:

$$f = -\left(\frac{\mu}{k+0.5\mu w_{crk}\beta_w}\right)u \tag{2}$$

where μ is the viscosity, $k = w_{crk}^2/12$ is the crack permeability (where $w_{crk}(\chi, t)$ is the crack width, for which the dependencies have been dropped for clarity), β_w (with units m³/Ns) is a wall slip factor. [43,44,71]

The governing mass balance equation is given by:

$$\frac{\partial(\rho_h A)}{\partial t} + \frac{\partial(\rho_h A u)}{\partial \chi} + \rho_h A Q_{crk} = 0 \quad \forall \mathbf{x} \in \Omega_{crk} \tag{3}$$

where A is the flow channel area (here taken as $w_{crk} \times 1$).

In the present work, the coupling between flow in the discrete cracks and the concrete matrix is dealt with in a similar manner to an embedded discrete fracture model.[72-75] The embedded discrete fracture flow model, originally proposed by Lee et al.[72] (see also Li and Lee)[73] employs separate domains for the matrix and the crack (which may cross the underlying matrix mesh arbitrarily). The two are coupled through transfer functions which describe the mass flux between the two domains. Here, the mass flux between the crack faces and the matrix is described as follows:[72,76]

$$Q_{crk} = -\frac{2}{\rho_h}n\beta_{crk}(P_h - P_{hcrk}) \quad \forall \mathbf{x} \in \Gamma_i \tag{4}$$

where β_{crk} (which has units of s/m) is a boundary transfer coefficient, n is the porosity of the surrounding matrix and P_h and P_{hcrk} are the pressures of the healing agent in the matrix and the crack respectively. The factor 2 is included to take into account flow through both crack faces (it is noted that in the case of different matrix pressures on each side of the crack, Q_{crk} would be calculated as the sum of fluxes through each crack face).

The total driving pressure for the crack flow (P) consists of the capillary pressure, a term to account for frictional dissipation at the meniscus (β_m with units Ns/m², applied at the free surface),[43,44,77] and an applied pressure from the vascular network, as follows:

$$P = P_c(\theta_d)(1 - \beta_s) - 2\frac{\beta_m}{w_{crk}}u + P_{app} \tag{5}$$

where β_s is a factor to allow for pinning of the meniscus.[43,44,78]

Equations (1) and (3) form a coupled system to be solved for velocity and pressure. Application of the finite element method to this system requires the satisfaction of the inf-sup condition to ensure stability of the formulation,[79] often achieved by using different orders of interpolation for the velocity and pressure. In the present work, however, equal order interpolations are preferred and stability is ensured using a continuous interior penalty method following the approach of Burman et al.[79] (see also Claus and Kerfriden,[80]).

Continuum matrix flow

Fluid flow in a partially saturated porous medium is governed by the mass balance equations for the liquid, liquid vapour and dry air. In this study it is assumed that the combined effect of liquid and vapour transport can be captured through a single effective diffusion coefficient. It is also assumed that the medium is dry, such that there is no moisture (water) in the capillary pores and that the gas pressure remains constant at atmospheric pressure, following the approach of Chitez and Jefferson.[42] The mass balance equation governing continuum matrix flow of the healing agent is given by:[42,81,82]

$$\frac{\partial(\overline{\rho_h})}{\partial t} + \mathbf{\nabla} \cdot \mathbf{J}_h + Q_{mtx} = 0 \quad \forall \, \mathbf{x} \in \Omega_{mtx} \tag{6}$$

where $\overline{\rho_h} = \rho_h n S_h$ is the phase averaged density (S_h is the degree of saturation), Q_{mtx} is a source/sink term and $\mathbf{J}_h$ is the healing agent flux given as:

$$\mathbf{J}_h = -\rho_h K_{eff}(S_h)(\mathbf{\nabla}P_h - \rho_h\mathbf{g}) \tag{7}$$

where $P_h = P_g - P_c$ is the healing agent pressure (P_g is the gas pressure) and K_{eff} is an effective diffusion coefficient based on Darcy's law:[42,81,82]

$$K_{eff}(S_h) = \frac{K_{int}K_{hrel}(S_h)}{\mu} \tag{8}$$

where K_{int} is the intrinsic permeability of the medium and K_{hrel} is the relative permeability which depends on the degree of saturation according to the well-known van Genuchten-Mualem relationship:[42,83-85]

$$K_{hrel}(S_h) = S_h{}^\kappa \left[1 - \left(1 - S_h^{\frac{1}{m}}\right)^m\right]^2 \tag{9}$$

where κ is the pore interaction factor which accounts for the connectivity and tortuosity of the pores.

S_h is related to the capillary pressure by van Genuchten's moisture retention function,[84] as follows:

$$P_c(S_h) = a\left(S_h^{-1/m} - 1\right)^{1-m} \tag{10}$$

where a and m are constants that depend on the medium.

The source/sink term in equation (6) is associated with the embedded discrete cracks and is given as follows:[76]

$$Q_{mtx} = \mathbf{J}_\Gamma \cdot \mathbf{n}_\Gamma = 2n\beta_{crk}(P_h - P_{hcrk}) \quad \forall \, \mathbf{x} \in \Gamma_i \tag{11}$$

where Γ_i represents the internal boundary.

3 Numerical Solution

Boundary conditions

In order to solve the system of equations (1, 3 & 6), initial and boundary conditions are required. The initial conditions give the values of the variables at time $t = t_0$ and are given by:

$$u = u^0, P_{hcrk} = P_{hcrk}^0 \quad \forall \, \mathbf{x} \in \Omega_{crk} \tag{12}$$

$$P_h = P_h^0 \qquad\qquad \forall \, \mathbf{x} \in \Omega_{mtx} \tag{13}$$

The boundary conditions are of the Cauchy and Dirichlet type. The Cauchy type describe the rate of mass transfer from the environment to the sample and are given by:

$$\mathbf{J}_q \cdot \mathbf{n} - q_h - \beta_c(P_h - P_{henv}) = 0 \quad \forall \mathbf{x} \in \Gamma_{mtx,c} \tag{14}$$

where q_h is the healing agent flux, $\mathbf{n}$ is the unit normal vector to the boundary and $\Gamma_{mtx,c} \subseteq \Gamma_{mtx}$ represents the part of Γ_{mtx} to which Cauchy boundary conditions are applied.

The Dirichlet boundary conditions are given by:

$$u(t) = u^\Gamma, P_{hcrk}(t) = P_{hcrk}^\Gamma \quad \forall \mathbf{x} \in \Gamma_{crk,d} \tag{15}$$

$$P_h(t) = P_h^\Gamma \quad \forall \mathbf{x} \in \Gamma_{mtx,d} \tag{16}$$

where $\Gamma_{crk,d} \subseteq \Gamma_{crk}$ represents the part of Γ_{crk} to which Dirichlet boundary conditions are applied and $\Gamma_{mtx,d} \subseteq \Gamma_{mtx}$ is defined similarly.

At the free surface of the fluid in the crack, the jump in fluid stress across the interface is balanced by the capillary pressure:

$$\left[\!\left[\mathbf{n}_f \cdot \mathbf{T} \cdot \mathbf{n}_f\right]\!\right] = P_c \quad \forall \mathbf{x} \in \Gamma_{crk,f} \tag{17}$$

where $\left[\!\left[\cdot\right]\!\right]$ is the jump operator, $\mathbf{n}_f$ denotes the unit normal to the free surface, $\Gamma_{crk,f} \subseteq \Gamma_{crk}$ denotes the part of Γ_{crk} which is a free surface and $\mathbf{T}$ is the stress tensor which is given by (where $\mathbf{v}$ is the fluid velocity vector):

$$\mathbf{T} = \mu(\nabla\mathbf{v} + (\nabla\mathbf{v})^\mathrm{T}) - P_{hcrk}\mathbf{I} \tag{18}$$

where $\mathbf{I}$ denotes the identity matrix. For Poisueille flow, the term in the jump operator in equation (17) is given by:

$$\mathbf{n}_f \cdot \mathbf{T} \cdot \mathbf{n}_f = 2\mu\frac{\partial v_\chi}{\partial \chi} - P_{hcrk} \tag{19}$$

where v_χ denotes the fluid velocity in the direction of the convected coordinate.

taking the average over the interface length and inserting into (17) leads to:

$$\left[\!\left[2\mu\frac{\partial u}{\partial \chi} - P_{hcrk}\right]\!\right] = P_c \tag{20}$$

In the present work, the first term on the left-hand-side of equation (20) was found to be negligible in comparison with the second and was therefore not included.

Finite element formulation and solution method

The governing equations for crack and matrix flow describe a nonlinear system to be solved that are coupled through the sink/source term. The primary variables are the flow velocity in the crack and the healing agent pressure in the crack and in the matrix. Introducing the space for the trial functions as $U = \{\hat{\mathbf{u}} \in H^1(\Omega)|\hat{\mathbf{u}}(\mathbf{x}) = \mathbf{\Phi}^\Gamma \; \forall \mathbf{x} \in \Gamma_d\}$, and employing the Gauss-Green divergence theorem, the weak form of the governing equations becomes:

find $\mathbf{\Phi} \in U$, such that:

$$\int_{\Omega_{crk}} \mathbf{W}^\mathrm{T}\left(\frac{\partial u}{\partial t} + u\frac{\partial u}{\partial \chi} + \frac{1}{\rho_h}f + \frac{1}{\rho_h}\frac{\partial P_{hcrk}}{\partial \chi} - gsin\phi\right) d\Omega_{crk} + \int_{\Gamma_i} \mathbf{W}^\mathrm{T}(uQ_{crk}) d\Gamma_i + \int_{\Gamma_{crk,f}^e} \mathbf{W}^\mathrm{T}\left(P_{hcrk} + P_c - 2\frac{\beta_m}{w_{crk}}u\right) d\Gamma_{crk,f}^e = 0 \tag{21}$$

$$\int_{\Omega_{crk}} \mathbf{W}^\mathrm{T}\left(\frac{\partial A}{\partial t} + \frac{\partial(Au)}{\partial \chi}\right) d\Omega_{crk} + \int_{\Gamma_i} \mathbf{W}^\mathrm{T}(AQ_{crk}) d\Gamma_i = 0 \tag{22}$$

$$\int_{\Omega_{crk}} \mathbf{W^T} \left(\frac{\partial \overline{\rho_h}}{\partial t}\right) d\Omega_{crk} + \int_{\Omega_{crk}} \nabla \mathbf{W^T} \left(\rho_h \frac{K_{int} K_{hrel}}{\mu} \nabla P_h - \rho_h \frac{K_{int} K_{hrel}}{\mu} \rho_h \mathbf{g}\right) d\Omega_{crk} + \int_{\Gamma_{mtx,c}} \mathbf{W^T} \left(q_h + \beta_c (P_h - P_{henv})\right) d\Gamma_{mtx,c} +$$
$$\int_{\Gamma_i} \mathbf{W^T} (Q_{mtx}) d\Gamma_i = 0 \tag{23}$$

where $\mathbf{\Phi}$ is the vector of unknowns and $\mathbf{W}$ is the vector of weight functions.

In the present work, the Galerkin weighted residual method is employed for the spatial discretisation. The resulting system of equations is as follows:

$$\begin{bmatrix} \mathbf{C}_{11} & 0 & 0 \\ 0 & 0 & 0 \\ 0 & 0 & \mathbf{C}_{33} \end{bmatrix} \begin{bmatrix} \dot{\overline{\mathbf{u}}} \\ \dot{\overline{\mathbf{P}}}_{\mathrm{hcrk}} \\ \dot{\overline{\mathbf{P}}}_{\mathrm{h}} \end{bmatrix} + \begin{bmatrix} \mathbf{K}_{11} & \mathbf{K}_{12} & 0 \\ \mathbf{K}_{21} & \mathbf{K}_{22} & 0 \\ 0 & 0 & \mathbf{K}_{33} \end{bmatrix} \begin{bmatrix} \overline{\mathbf{u}} \\ \overline{\mathbf{P}}_{\mathrm{hcrk}} \\ \overline{\mathbf{P}}_{\mathrm{h}} \end{bmatrix} = \begin{bmatrix} \mathbf{F}_1 \\ \mathbf{F}_2 \\ \mathbf{F}_3 \end{bmatrix} \tag{24}$$

where the superior dot denotes the time derivative and the primary variables are interpolated from the nodal values by:

$$u = \boldsymbol{\zeta} \overline{\mathbf{u}}, \qquad P_{hcrk} = \boldsymbol{\zeta} \overline{\mathbf{P}}_{\mathrm{hcrk}}, \qquad P_h = \boldsymbol{\varsigma} \overline{\mathbf{P}}_{\mathrm{h}} \tag{25}$$

where $\boldsymbol{\zeta}$ and $\boldsymbol{\varsigma}$ are vectors of shape functions for the domains Ω_{crk} and Ω_{mtx} respectively.

The global matrices are given by:

$$\mathbf{C}_{11} = \sum_{e=1}^{nec} \int_{\Omega_{crk}^e} \boldsymbol{\zeta}^{\mathbf{T}} \boldsymbol{\zeta} \, d\Omega_{crk}^e \tag{26}$$

$$\mathbf{C}_{33} = \sum_{e=1}^{nem} \int_{\Omega_{mtx}^e} \boldsymbol{\varsigma}^{\mathbf{T}} \left(\frac{\partial \overline{\rho_h}}{\partial P_h}\right) \boldsymbol{\varsigma} \, d\Omega_{mtx}^e \tag{27}$$

$$\mathbf{K}_{11} = \sum_{e=1}^{nec} \left(\int_{\Omega_{crk}^e} \boldsymbol{\zeta}^{\mathbf{T}}(u) \nabla \boldsymbol{\zeta} \, d\Omega_{crk}^e + \int_{\Omega_{crk}^e} \boldsymbol{\zeta}^{\mathbf{T}} \left(\frac{1}{\rho_h} \frac{\mu}{k + 0.5 \mu w_{crk} \beta_w}\right) \boldsymbol{\zeta} \, d\Omega_{crk}^e \right) \tag{28}$$

$$\mathbf{K}_{12} = \sum_{e=1}^{nec} \left(\int_{\Omega_{crk}^e} \boldsymbol{\zeta}^{\mathbf{T}} \left(\frac{1}{\rho_h}\right) \nabla \boldsymbol{\zeta} \, d\Omega_{crk}^e + \int_{\Gamma_{crk,f}^e} \boldsymbol{\zeta}^{\mathbf{T}} \boldsymbol{\zeta} \, d\Gamma_{crk,f}^e \right) \tag{29}$$

$$\mathbf{K}_{21} = \sum_{e=1}^{nec} \int_{\Omega_{crk}^e} \boldsymbol{\zeta}^{\mathbf{T}} \nabla \boldsymbol{\zeta} \, d\Omega_{crk}^e \cdot A \mathbf{I} \tag{30}$$

$$\mathbf{K}_{22} = j_p \sum_{ed=1}^{E_{Gi}} \left(\frac{h^3}{\mu} \left(\int_{E^{ed}} [[\nabla \boldsymbol{\zeta}^{\mathbf{T}}]]_E \nabla \boldsymbol{\zeta}_{K_+} \, dE^{ed} - \int_{E^{ed}} [[\nabla \boldsymbol{\zeta}^{\mathbf{T}}]]_E \nabla \boldsymbol{\zeta}_{K_-} \, dE^{ed} \right) \right) \tag{31}$$

$$\mathbf{K}_{33} = \sum_{e=1}^{nem} \int_{\Omega_{mtx}^e} \nabla \boldsymbol{\varsigma}^{\mathbf{T}} \left(\rho_h \frac{K_{int} K_{hrel}}{\mu}\right) \nabla \boldsymbol{\varsigma} \, d\Omega_{mtx}^e \tag{32}$$

$$\mathbf{F}_1 = \sum_{e=1}^{nec} \left(\begin{array}{c} \int_{\Omega_{crk}^e} \boldsymbol{\zeta}^{\mathbf{T}}(g \sin\phi) \, d\Omega_{crk}^e + \int_{\Gamma_i^e} \boldsymbol{\zeta}^{\mathbf{T}} \left(u \frac{2}{\rho_h}(\beta_{crk} n(P_h - P_{hcrk}))\right) d\Gamma_i^e + \\ \int_{\Gamma_{crk,f}^e} \boldsymbol{\zeta}^{\mathbf{T}} \left(-P_c + 2\frac{\beta_m}{w_{crk}} u\right) d\Gamma_{crk,f}^e \end{array} \right) \tag{33}$$

$$\mathbf{F}_2 = \sum_{e=1}^{nec} \left(-\int_{\Omega_{crk}^e} \boldsymbol{\zeta}^{\mathbf{T}} \left(\frac{\partial A}{\partial t}\right) d\Omega_{crk}^e + \int_{d\Gamma_i^e} \boldsymbol{\zeta}^{\mathbf{T}} \left(A \frac{2}{\rho_h}(\beta_{crk} n(P_h - P_{hcrk}))\right) d\Gamma_i^e \right) \tag{34}$$

$$\mathbf{F}_3 = \sum_{e=1}^{nem} \left(\int_{\Omega_{mtx}^e} \nabla \boldsymbol{\varsigma}^{\mathbf{T}} \left(\rho_h \frac{K_{int} K_{hrel}}{\mu} \rho_h \mathbf{g}\right) d\Omega_{mtx}^e - \int_{\Gamma_{mtx,c}^e} \boldsymbol{\varsigma}^{\mathbf{T}} (q_h + \beta_c n(P_h - P_{henv})) d\Gamma_{mtx,c}^e - \int_{\Gamma_i^e} \boldsymbol{\varsigma}^{\mathbf{T}} (2\beta_{crk} n(P_h - P_{hcrk})) d\Gamma_i^e \right) \tag{35}$$

It can be noted that in the above, the particular form of the matrix $\mathbf{K}_{21}$ was preferred as this form requires no partial differentiation of the mass flux, $\partial(uA)/\partial\chi$ (which could lead to errors due to the dependence of u on A). The matrix $\mathbf{K}_{22}$ arises from the continuous interior penalty employed to stabilise the Navier-Stokes equations, which is elaborated in the next section.

Equation (24) can be written in the following compact form:

$$\check{\mathbf{K}} \mathbf{\Phi} + \check{\mathbf{C}} \dot{\mathbf{\Phi}} = \check{\mathbf{F}} \tag{36}$$

Applying an implicit Euler backward difference scheme for the time discretisation leads to:[81]

$$\check{\mathbf{K}}\boldsymbol{\Phi}^{t+1} + \frac{1}{\Delta t}\check{\mathbf{C}}(\boldsymbol{\Phi}^{t+1} - \boldsymbol{\Phi}^{t}) = \check{\mathbf{F}} \tag{37}$$

Due to the different time scales associated with the matrix and crack flows (the crack flow, in general, occurs at a much higher rate than the matrix flow due to the applied pressure and much higher equivalent permeability), the equations are solved in a sequential manner, with a sub-stepping procedure being employed for the crack flow.

In the present work, the free surface stress balance condition as well as the interior penalty applied to the discrete crack flow equations are dealt with implicitly. The nonlinear convection and source/sink terms found in the Navier-Stokes equations, are accounted for using a Picard iteration that computes the new approximation from:

$$\boldsymbol{\Phi}^{t+1}_{k+1} = (\Delta t\check{\mathbf{K}} + \check{\mathbf{C}})^{-1}(\Delta t\check{\mathbf{F}} + \check{\mathbf{C}}\boldsymbol{\Phi}^{t}) \quad \forall\, \mathbf{x} \in \Omega_{crk} \tag{38}$$

where the nonlinear terms are linearised as:[80]

$$u^{k+1}\frac{\partial(u^{k+1})}{\partial\chi} \approx u^{k}\frac{\partial(u^{k+1})}{\partial\chi}, \; u^{k+1}Q_{crk}(P^{k+1}_{hcrk}) \approx u^{k}Q_{crk}(P^{k}_{hcrk}) \tag{39}$$

where k denotes the iteration number.

The nonlinearity of the continuum matrix flow is dealt with using a standard Newton-Raphson procedure,[81] which gives the following iterative update of the solution, as follows:

$$\delta\boldsymbol{\Phi}^{t+1}_{k+1} = \left[\frac{\partial\boldsymbol{\xi}}{\partial\boldsymbol{\Phi}^{t+1}_{k}}\right]^{-1}(-\boldsymbol{\xi}) \quad \forall\, \mathbf{x} \in \Omega_{mtx} \tag{40}$$

where $\boldsymbol{\xi}$ is the approximation error given by:

$$\boldsymbol{\xi} = \Delta t\check{\mathbf{K}}\boldsymbol{\Phi}^{t+1} + \check{\mathbf{C}}(\boldsymbol{\Phi}^{t+1} - \boldsymbol{\Phi}^{t}) - \Delta t\check{\mathbf{F}} \quad \forall\, \mathbf{x} \in \Omega_{mtx} \tag{41}$$

The iterative updates are terminated once the norm of the error meets a defined tolerance.

Stabilisation

The stabilisation term, j, for the Navier-Stokes equations is given as a penalty on the jump in pressure gradient over element edges:[80]

$$j(\mathbf{P}_{hcrk}) = j_{p}\sum_{ed=1}^{E_{Gi}}\frac{h^{3}}{\mu}\int_{E^{ed}}[[\nabla\mathbf{P}_{hcrk}]]_{E}[[\nabla\boldsymbol{\zeta}]]_{E}dE^{ed} \tag{42}$$

where j_{p} is the stabilisation parameter, h is the local mesh size, E denotes an element edge and E_{Gi} denotes the global set of interior element edges. $[[\nabla x]]_{E}$ denotes the jump of ∇x across an edge shared by two elements, K_{+} and K_{-} defined as $[[\nabla x]]_{E} = \nabla x_{K_{+}}\mathbf{n}_{E} - \nabla x_{K_{-}}\mathbf{n}_{E}$, where $\mathbf{n}_{E}$ denotes the unit normal to the edge E.

The jump in pressure across an element edge is given by:

$$[[\nabla\mathbf{P}_{hcrk}]]_{E} = \nabla\boldsymbol{\zeta}_{K_{+}}\mathbf{P}_{hcrk,K_{+}}\mathbf{n}_{E} - \nabla\boldsymbol{\zeta}_{K_{-}}\mathbf{P}_{hcrk,K_{-}}\mathbf{n}_{E} \tag{43}$$

where $\nabla\boldsymbol{\zeta}_{i}$ and $\mathbf{P}_{hcrk,i}$ represent the vector of shape function derivatives and the vector of nodal pressures for element i respectively. For further details of this scheme, the interested reader is referred to Burman et al.[79]

Due to the highly nonlinear dependence of the permeability on the degree of saturation (which in turn depends on liquid pressure), equation (6) is subject to numerical oscillations, particularly for sharp wetting fronts into a dry medium. This issue was addressed in detail for 1D elements by Pan et al.,[86] who examined the difference between the neighbouring node response function (NNRF) for mass-distributed and mass-

lumped matrices (noting that oscillations are not found for linear elements when mass-lumped matrices are used). The issue with using mass-lumped matrices is that the numerical predictions become over-diffusive since an increase in moisture content at the drier node is always predicted independently of the position of the moisture front. To address this, Pan et al.[86] proposed new shape functions for the storage matrices that were a function of a factor (α). This factor was derived from the NNRF and ensures that the response at the drier node is either positive or zero (mass-lumped schemes always predict a positive response, whilst mass-distributed sometimes predict a negative response).

In the present work, a different approach is employed, in which the storage matrix is computed as an interpolation between the mass-distributed and mass-lumped matrices. This is similar to the approach of Mirbagheri et al.[87] who applied a higher order mass matrix to a discontinuous wave propagation problem to dampen spurious oscillations (see also Wu and Qiu,[88] and Wang et al.[89]). This leads to:

$$\mathbf{C} = \alpha \mathbf{C}_{\mathrm{L}} + (1 - \alpha)\mathbf{C}_{\mathrm{D}} \tag{44}$$

where $\mathbf{C}$ denotes the storage matrix for continuum matrix flow, the L and D subscripts refer to mass-lumped and mass-distributed matrices respectively and the weighting factor α is calculated such that the change in liquid pressure at a downstream node is greater than or equal to zero (or to the mass sink where appropriate) following the approach of Pan et al.[86] and is given by:

$$\alpha = 1 - \min\left(1, \frac{\left|\sum_{j=1}^{nd} \mathbf{K}_{33_{i,j}} \mathbf{P}_{h_j}\right|}{\left|\sum_{j=1}^{nd} \mathbf{C}_{33_{i,j}} \frac{\Delta \mathbf{P}_{h_j}}{\Delta t}\right|}\right) \tag{45}$$

where the subscript i denotes the driest node.

This method prevents the occurrence of any spurious oscillations whilst reducing smearing of the wetting front.

Interface tracking

For the crack flow, the spatial discretisation within the crack needs to account for the transient movement of the free-surface of the fluid. Two approaches were considered for this, namely, the fixed mesh approach and the adaptive mesh approach.[90] The former defines a mesh that does not move with or adapt to the fluid surface, in which case, it is necessary to track the movement of the surface within the mesh using, for example, a level set method.[91] In the latter approach, the fluid surface lies on element boundaries. Thus, it is necessary to update the mesh adjacent to the fluid surface whenever it moves. However, a true fixed mesh approach is not applicable to problems with evolving cracks and because adapting the mesh adjacent to the surface is straightforward in a 1D situation the moving mesh approach, illustrated in Figure 2, was employed in this work. The essential steps of the algorithm are as follows:

1. The mechanics problem is solved, which gives the position and widths of the macro-cracks. These macro-cracks act as potential flow paths for the healing agent.
2. The Navier-Stokes equations (eqns. 1 & 3) are solved for the velocities, u, and pressures, P_{hcrk}.
3. The movement of the interface over a time step is calculated:[52,91]
$$\lambda^{t+\Delta t} = \lambda^t + \Delta t u_\lambda$$

    where λ denotes the total accumulated length of flow within the crack.

4. If the interface crosses an element boundary (from the continuum element edge), a node is placed at this position.

The algorithm is illustrated in Figure 2, in which the quadrilateral elements indicate the underlying matrix mesh, the black circles (crack nodes) connected by the dashed lines indicate the crack flow mesh.
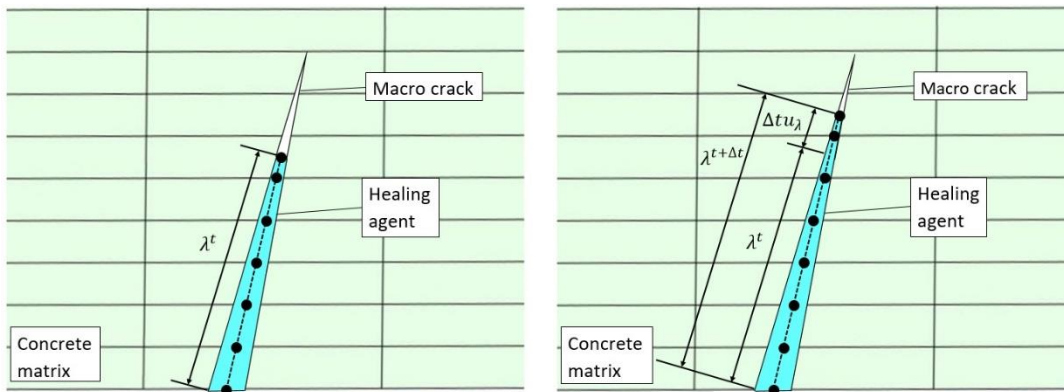
Figure 2 – Interface tracking and re-meshing over a time step

Algorithm

The algorithm for the model is given in Box 1. In the present work, it is assumed that the flow is initiated once a critical crack width is reached at the location of the capillary channels.

The mechanical and transport aspects of the model are solved sequentially, which is justified by the fact that the transport has no effect on the mechanical model, since the applied pressures are negligible with respect to the mechanical strength of the material.

Box 1 – Staggered solution algorithm

$t = t_0; \mathbf{F}_{load} = \mathbf{0}$	Initialise all cumulative variables
for itm=1 to ntm	Loop time steps
$\quad t_p = t$	Set previous time
$\quad t = t + \Delta t$	Increment the time variable
$\quad \mathbf{F}_{load} = \mathbf{F}_{load} + \Delta\mathbf{F}_{load}$	Increment loads
$\quad w_{crk} = w_{crkp}$	Extract crack widths for crack flow computations
$\quad$ **if** $w_{crk} > w_{crit}$	Check for crack flow
! Crack flow calculations	
$\quad$ **for** is=1 to ns	Loop sub steps for crack flow
$\quad ts = t_p + (is/nsub)\Delta t$	Sub time increment
$\quad\quad \theta_d$	Calculate DCA (eqn. 47)
$\quad\quad$ **for** ict=1 to nct	Enter crack flow iteration loop
$\quad\quad\quad Q_{crk}, Q_{mtx}$	Calculate source/sink term (eqns. 4 & 11)
$\quad\quad\quad \boldsymbol{\omega}_{k+1}^{t+1} = (\Delta t \breve{K} + \breve{C})^{-1}(\Delta t \breve{F} + \breve{C}\boldsymbol{\omega}^t)$	Solve for crack flow variables
$\quad\quad\quad$ **if** $|\Delta\boldsymbol{\omega}|/\omega_{ref} < tol_\omega$ **exit**	Check convergence
$\quad\quad$ **endfor** ict	
$\quad\quad \lambda^{t+1} = \lambda^t + \Delta t u_\lambda$	Advect front position
$\quad\quad$ **call** meshupdate	Update 1D crack flow mesh
$\quad$ **endfor** is	
! end crack flow calculations	
$\quad$ **for** it=1 to nt	Enter iteration loop
! Mechanical calculations	
$\quad\quad \delta\mathbf{d}_{k+1}^{t+1} = \left[\frac{\partial\boldsymbol{\xi}_d}{\partial\mathbf{d}_k^{t+1}}\right]^{-1}(-\boldsymbol{\xi}_d)$	Solve for increment of displacements
$\quad\quad \mathbf{d} = \mathbf{d} + \delta\mathbf{d}$	Update displacements
! end mechanical calculations	
! Matrix flow calculations	
$\quad\quad \delta\mathbf{P}_{h,k+1}^{t+1} = \left[\frac{\partial\boldsymbol{\xi}_P}{\partial\mathbf{P}_{h,k}^{t+1}}\right]^{-1}(-\boldsymbol{\xi}_P)$	Solve for increment of healing agent pressure
$\quad\quad \mathbf{P}_h = \mathbf{P}_h + \delta\mathbf{P}_h$	Update healing agent pressure
! end matrix flow calculations	
$\quad\quad$ **if** $|\delta\mathbf{d}|/d_{ref} < tol_d \ \wedge |\delta\mathbf{P}_h|/P_{h,ref} < tol_P$ **exit**	Check convergence
$\quad$ **endfor** it	
endfor itm	

in which;

$\quad w_{crit}$ is a critical crack width after which crack flow is initiated

$\quad \mathbf{F}_{load}$ is the mechanical load vector

$\quad \boldsymbol{\omega}$ is the vector of velocities and pressures for the crack flow

$\quad \omega_{ref}, d_{ref}$ and $P_{h,ref}$ are reference vectors for normalising $\boldsymbol{\omega}$, $\mathbf{d}$ and $\mathbf{P}_h$ respectively

$\quad$ ntm, ns, and nt are the number of time steps, sub steps and limiting number of iterations for the matrix flow respectively

$\quad tol_\omega, tol_d$ and tol_p are the tolerances for $\boldsymbol{\omega}$, $\mathbf{d}$ and $\mathbf{P}_h$ respectively

Effect of inertia

The inertial terms in equation (1) (i.e. $\partial(\rho u)/\partial t$ and $u\partial(\rho u)/\partial \chi$) are neglected in many numerical models due to their minimal influence on the overall flow behaviour. Whilst this is justified in many cases, in the present application, in which the healing agent can be pressurised to drive it into the cracks and the crack widths can become relatively wide (reducing viscous resistance), these terms can become non-negligible. To demonstrate this, a hypothetical test case is considered that concerns the rise of CA in a vertical crack. The test conditions were chosen to represent a large-scale concrete structure in which cracks can become relatively wide (>0.5mm) and long (>1m). For this illustrative example, a non-uniform crack was chosen, with a width of 1 mm at the healing-agent source, a taper of 0.0001 mm/mm and a source pressure of 1.0 bar. The comparison between numerical predictions with and without the inertial terms is given in Figure 3. The parameters used in the simulation can be seen in Table 1.
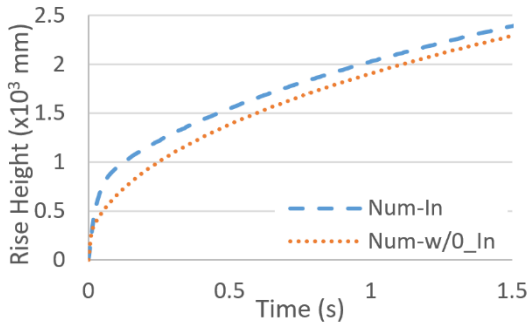
Figure 3 – Comparison of predicted capillary rise height with and without inertial terms

Table 1 – CA properties

Parameter	Value
γ (N/m)	0.033
ρ_h (kg/m^3)	1060
μ (Ns/m^2)	0.004
θ_s (rad)	0.175

It may be seen from the figure that the inertial terms have a significant effect on the predicted response in this case and thus should not always be neglected.

4 Dynamic Contact Angle

The driving force for the healing agent flow within a discrete crack is made up of any applied pressure and the meniscus force. The meniscus force is a function of the surface tension and the curvature of the liquid-air interface. The equivalent capillary pressure is equal to the difference in pressure between two fluids (healing agent and air in the present case) and is given by the Young-Laplace equation:[92]

$$P_c = \frac{2\gamma \cos(\theta_d - \sigma)}{w_{crk}}$$

(46)

where γ is the surface tension of the healing agent, σ is the inclination of the capillary wall (measured relative to the crack inclination) and θ_d is the dynamic contact angle (DCA).

The contact angle varies significantly with velocity and this variation can have a marked effect on the fluid behaviour.[64,93] In fact, if the velocity is sufficiently large to cause the dynamic contact angle to exceed 90°, which is possible in the present healing system, the meniscus force resists, rather than drives, flow.

A number of models have been proposed for the dependence of the contact angle on the capillary number (where the capillary number is given by: $Ca = \mu u/\gamma$), including models based on molecular kinetics,[94] hydrodynamic theory,[95] empirical observations or combinations of these approaches.[96] Here, three particularly convenient models are selected for comparison, namely the models due to Jiang et al.,[97] Bracke et al.,[98] and Cox.[95] The governing relationships for these three models are as follows:

Jiang et al.:[97]

$$tanh(c_1 Ca^{c_2}) = \frac{cos(\theta_s) - cos(\theta_d)}{cos(\theta_s) + 1} \tag{47}$$

Bracke et al.:[98]

$$c_1 Ca^{c_2} = \frac{cos(\theta_s) - cos(\theta_d)}{cos(\theta_s) + 1} \tag{48}$$

Simplified Cox:[95]

$$\theta_d^{c_2} - \theta_s^{c_2} = c_1 Ca \tag{49}$$

where θ_s is the static contact angle and c_1 and c_2 are constants.

In order to assess the applicability of the above DCA relationships to the dynamic flow of CA, Selvarajoo et al.,[99] carried out a series of experiments at Cardiff University on the flow of healing agent through glass tubes under different pressures. In these tests, flexible tubes were placed at either side of a capillary tube with one end connected to an air-line (to apply pressure), and the other (open) end directing the CA into a plastic container filled with sand. LED lights were placed at either side of the set up to illuminate the tube. The flow was recorded using a high-speed camera and the contact angles were measured at different flow rates using the software Image-J. The test set up is illustrated in Figure 4.
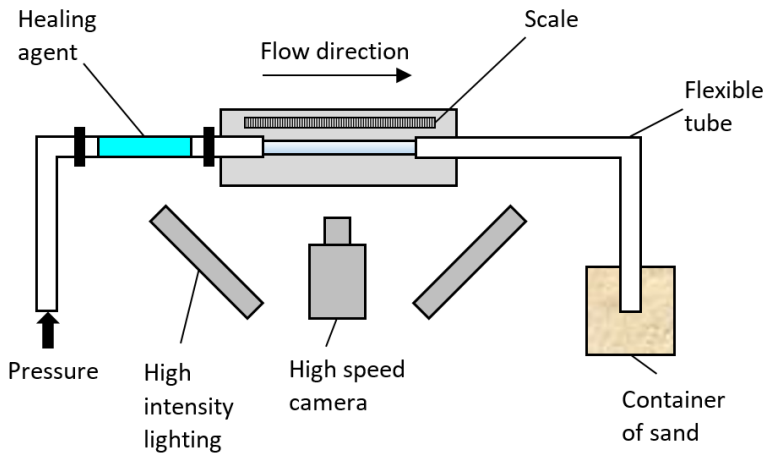

Figure 4 – Schematic of the DCA test set up of Selvarajoo et al.[99]

A comparison between predictions with the above three expressions and the experimental data is given in Figure 5. The values for the DCA constants for each formula are given in Table 2 and the CA properties used for the simulations were those given in Table 1. The applied pressure range considered was from 0.0 to 2.0 bar.

Table 2 – Calibrated parameters for DCA models

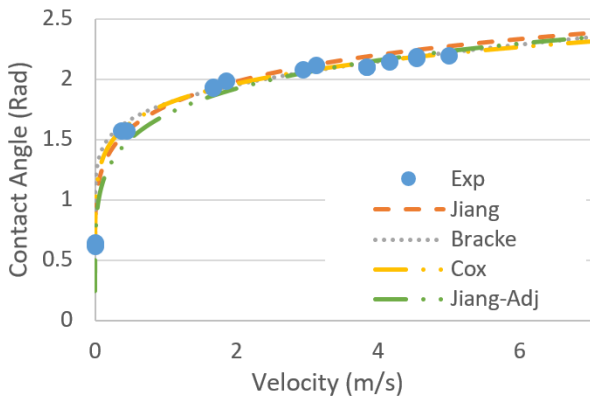| Model	c_1	c_2
Jiang et al. 1979	1.325	0.35
Bracke et al. 1989	0.8621	0.1947
Simplified Cox, 1986	722.9	7.654

Figure 5 – Calibration of DCA models against experimental data

It can be seen from the figure that all three models provide a good fit to the experimental data. Here, the model of Jiang et al.[97] is chosen since the function is asymptotic to π (with increasing u), which is the maximum physically meaningful contact angle. It can be noted that the above data related to CA on a glass substrate, whereas in the examples considered, the substrate is concrete. The contact angle is a measure of the wettability, which depends on the physiochemical properties of the fluid and substrate. To account for the difference in substrate, the static contact angle was adjusted using values reported in Gardner et al.[45] for CA on concrete.[99] The effect of this adjustment on the dynamic contact angle can be seen in Figure 5. In the present work, the constants, c_1 and c_2, in the DCA expressions are assumed to be independent of the substrate. It can be noted that the effect of differences in the substrate on the frictional dissipation and wall slip are taken into account in the model through the factors β_m and β_w respectively.[43,44] This issue is discussed further in Selvarajoo et al.[99]

To demonstrate the difference between a simulation that uses a DCA with one that employs a static contact angle, a hypothetical test case concerning the rise of CA in a vertical crack is considered. In this case the crack width was chosen as 0.1 mm and no external pressure was applied. The comparison of the numerical predictions with and without the DCA can be seen in Figure 6. The parameters used in the simulation are given in Table 1.
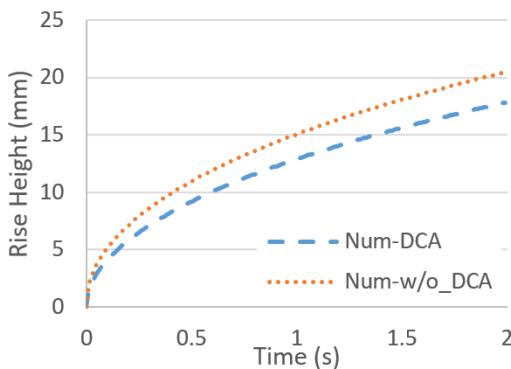

Figure 6 – Comparison of predicted capillary rise height with and without DCA

It can be seen from the figure that neglecting the DCA leads to a significant difference in the predicted rise heights.

5 Healing Agent Curing

Degree of cure

The curing of a significant class of adhesives is by a polymerisation reaction that is initiated by adsorbed moisture.[100] The curing is therefore dependent on moisture transport (or diffusion) within the adhesive body. For isocyanates and silicones, this diffusion process was found to exhibit a sharp propagating front that could be simulated accurately by Fick's diffusion law. Solving this diffusion equation with the appropriate boundary

conditions led to the following equation for the position of the diffusion front,[100] which may also be described in terms of the depth of cured material (z):

$$z = \left(2VK_pP_vt\right)^{\frac{1}{2}}$$ (50)

in which V is the volume of equivalent adhesive that reacts with 1 mole of water, K_p is the permeability of cured adhesive, P_v is the vapour pressure at the boundary and t is time.

The same polymerisation process applies to CA but in this case it has been found that the rate of propagation of the curing front gradually slows down as the depth of cured material increases and this zone of cured CA can eventually completely prevent hydroxide ions from reaching the central region of a layer of adhesive.[101] This finding resulted from a study on the curing characteristics of CA films of varying thickness on different substrates, which employed near Fourier transform infrared spectroscopy (FTIR) to measure the degree of cure. The Cambridge polymer group,[102] also used the FTIR technique to measure the degree of cure with time of CA droplets on glass slide substrates. Typical responses from both of these studies are shown in Figure 7.

Equation (50) does not well-represent the observed curing behaviour of CA due to the effects of the increasingly impermeable layer of cured CA, discussed above. Therefore, an alternative function was sought that can describe the progression of a CA curing front over time with reasonable accuracy. The function selected is given in equation (51) and its ability to represent the observed experimental behaviour is illustrated in Figure 7. It is noted that in the numerical results shown in Figure 7 are based on the assumption that the degree of cure (φ) may be calculated from $z(t)/z_{c0}$ in the two cases considered. This assumption is considered reasonable when a relatively narrow layer (or small droplet) of adhesive cures evenly from a smooth substrate. The selected function is expressed as:

$$z(t) = z_{c0}\left(1 - e^{\frac{-t}{\tau}}\right)$$ (51)

where z_{c0} is a critical curing depth at which the transport ceases and τ is a rate parameter (characteristic time).
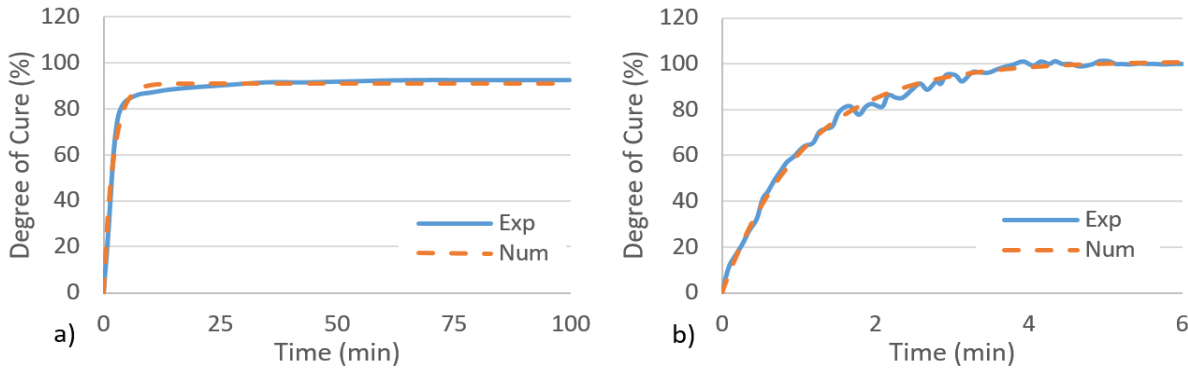

Figure 7 – Comparison of the predictions of the degree of cure with experimental data for a) 0.07mm film of CA on dental glass with $z_{c0} = 0.03192$ mm and $\tau = 2.079$ min,[101] and b) a droplet of CA on borosilicate glass with $z_{c0} = 0.5053$ mm and $\tau = 1.092$ min and assuming a droplet width of $2z_{c0}$.[102]

The above equation describes the progression of a sharp curing front, which has uncured material on one side and fully cured material on the other. However, in many situations the curing (or reaction) front is more diffuse,[99,103] as was clearly shown by Li et al.[103] in a series of experiments that studied the propagation of a polymerisation front of n-butyl CA adhesives mixed with an iodized oil in glass tubes. To determine the degree of polymerisation they used a grey-scale measurement of cure and found that the front was not sharp but took the form of a sigmoid function. Similarly, Selvarajoo et al.[99] found that a CA curing front adjacent to a cementitious substrate also becomes increasingly diffuse over time.

The transport of this type of reaction front can be described by the following advection diffusion equation (for equilibrium reactions):[104-106]

$$\frac{\partial \varphi_{x_c}}{\partial t} + v\frac{\partial \varphi_{x_c}}{\partial x_c} - D\frac{\partial^2 \varphi_{x_c}}{\partial x_c^2} = 0 \tag{52}$$

where x_c is a one-dimensional Cartesian coordinate measured from a defined boundary, φ_{x_c} is the degree of cure at a point, v is the advective velocity and D is the diffusion coefficient.

The solution of equation (52) (with a boundary condition of $\varphi_{x_c=0} = 1$), which treats the curing front as a moving interface with velocity v, is as follows:[104-106]

$$\varphi_{x_c}(x_c, t) = \frac{1}{2}\left(1 - erf\left(\frac{x_c - v \cdot t}{2\sqrt{Dt}}\right)\right) \tag{53}$$

where $v \cdot t$ gives the position of the interface.

Here, $v \cdot t$ is replaced by $z(t)$, which gives:

$$\varphi_{x_c}(x_c, t) = \frac{1}{2}\left(1 - erf\left(\frac{x_c - z(t)}{2\sqrt{Dt}}\right)\right) \tag{54}$$

The error function in equation (54) is non-elementary, which can be inconvenient from a numerical point of view, and so here a $tanh$ function is used as an approximation to the erf function, as illustrated in Figure 8,[107,108] which leads to the following equation for φ_{x_c}:

$$\varphi_{x_c}(x_c, t) = \frac{1}{2}\left(1 - tanh\left(\left(\frac{2}{\sqrt{\pi}}\right)\left(\frac{x_c - z(t)}{2\sqrt{Dt}}\right)\right)\right) \tag{55}$$

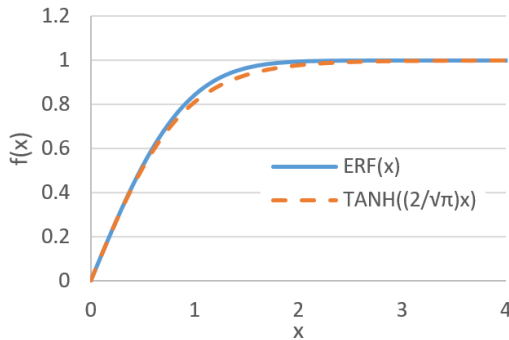Figure 8 – Comparison between $erf(x)$ and $tanh\left((2/\sqrt{\pi})x\right)$ functions

The problem with this function is that it predicts that the curing depth will continue to increase with time – without limit- due to the $2\sqrt{Dt}$ term, which is not consistent with the observations of Tomlinson et al.[101] or with our own observations.[99] To avoid this issue, we can instead use a term which is a function of z (which in turn is a function of time), as follows:

$$\varphi_{x_c}(x_c, t) = \frac{1}{2}\left(1 - tanh\left(\left(\frac{2}{\sqrt{\pi}}\right)\left(\frac{x_c - z(t)}{\sqrt{\frac{z(t)}{D}}}\right)\right)\right) \tag{56}$$

Finally introducing a wall factor gives:

$$\varphi_{x_c}(x_c, t) = \frac{1}{2}\left(1 - tanh\left(\left(\frac{2}{\sqrt{\pi}}\right)\left(\frac{x_c - z(t) - z_c}{z_c + \sqrt{\frac{z(t)}{D}}}\right)\right)\right) \tag{57}$$

where z_c is the wall factor.

To demonstrate the ability of the proposed function given in equation (57) to capture the curing profile of a CA adhesive, a comparison was made with the data from Li et al.,[103] which is given in Figure 9. The profile corresponds to the grey level measured at a selected time ($t = 62$ min) and assumes that the initial grey level (135) corresponds to the uncured material and the final value (90) relates to fully cured material. The comparison made here shows that equation (57) provides an adequate description of a typical curing profile. The parameters used in the simulation can be seen in Table 3.
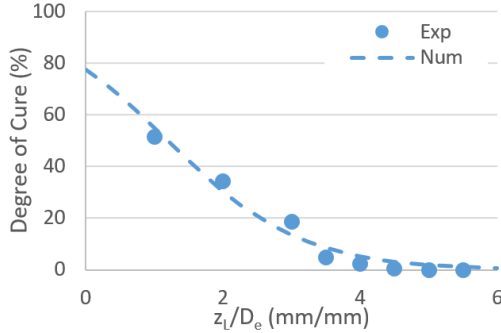

Figure 9 – Comparison between the predicted degree of cure profile and the measured data of Li et al.[103] at $t = 62$ min, where z_L denotes the distance from the interface and $D_e \approx 1.06$ mm denotes the diameter of the tube

Table 3 – Curing model parameters

Parameter	Value
z_{c0} (mm)	2.5
z_c (mm)	0.001
τ (min)	95
D (mm/ mm^2)	0.25

In order to determine the total degree of cure across the width of a crack, the integral of equation (57) is required, as follows:

$$\varphi(x_c, t) = \frac{x_c}{2} - \frac{1}{2} \ln \left(\cosh \left(\frac{\frac{2}{\sqrt{\pi}} x_c - \frac{2}{\sqrt{\pi}} z_c - \frac{2}{\sqrt{\pi}} z(t)}{z_c + \sqrt{\frac{z(t)}{D}}} \right) \right) \left(\frac{\sqrt{\pi}}{2} \sqrt{\frac{z(t)}{D}} + \frac{\sqrt{\pi}}{2} z_c \right) + c \tag{58}$$

where φ is the degree of cure between position x_c and 0 at time t.

The rate of cure of moisture-cure adhesives shows a strong dependence on the width of the adhesive sample. Tomlinson et al.[101] measured this effect for CA on dental glass and microscope slides. The experiments were carried out at a constant relative humidity of 40 % and temperature of 22.5 °C.

A comparison between selected data from Tomlinson et al's and predictions with the present curing model is given Figure 10, for which the parameters are given in Table 4. It may be noted that the two sets of parameters reflect the two boundaries, which are air at an RH of 40 % and the glass substrate.[101] It can be seen from the figure that the model captures the overall thickness dependency with reasonable accuracy although there are some notable differences between the numerical predictions of the curing rates and those observed in the experiments. The fact that the results for the thinnest film of CA suggest that the final degree of cure is below that for the next thinnest -in contrast to the overall trend- illustrates the variability (and difficulty of measuring) the curing process. It should be mentioned that for the case of a concrete crack, the boundary conditions are often equal on each side.
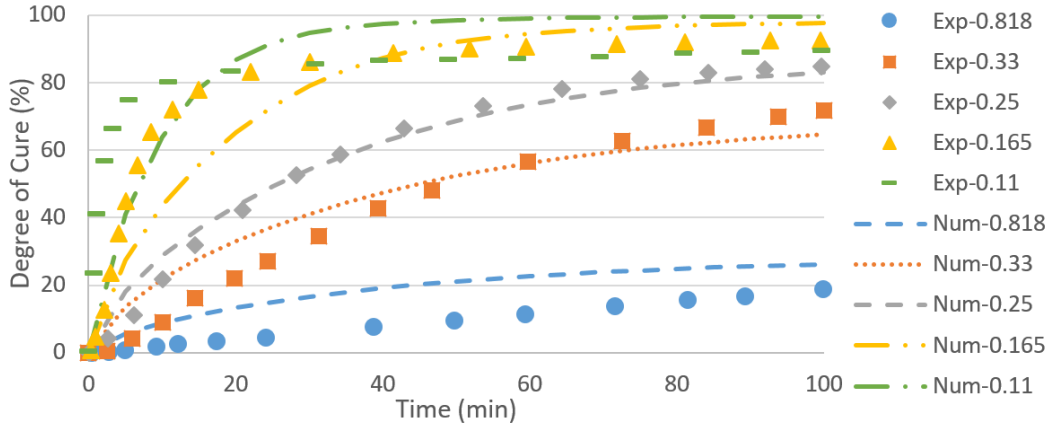
Figure 10 – Comparison of predictions of the degree of cure of different thicknesses of CA on a microscope slide with experimental data

Table 4 – Curing model parameters

Parameter (air)	Value	Parameter (glass)	Value
z_{c0} (mm)	0.2	z_{c02} (mm)	0.03
τ (s)	2400	τ_2 (s)	240
D (mm/ mm²)	100	D (mm/ mm²)	100
z_c (mm)	0	z_c (mm)	0

Rheology

As liquid healing agent cures, its viscosity increases until, at complete curing, it becomes a solid. Three approaches were considered to simulate this effect; the first uses a chemorheological model proposed by Castro and Macosko,[109] (See also, Ivankovic et al.[110] and Teyssandier et al.[111]), which describes the increase in viscosity with fractional conversion (or degree of cure), as:

$$\mu = \mu_0 \left(\frac{\varphi_g}{\varphi_g - \varphi} \right)^{nv} \tag{59}$$

where μ_0 is the initial viscosity, φ_g is the degree of cure at the gel point (where a rapid increase of viscosity is observed)[110] and nv is an exponent which defines the rate of change of μ with φ.

The second approach is based on the assumption that, during curing, the healing-agent can be idealised as a suspension of rigid spheres, with the spheres representing cured blocks of material and the liquid being the uncured agent. A mechanism that would justify this model is that, as the healing-agent flows through the crack under pressure and undergoes cycles of curing, re-damage and re-curing, particles of cured material break off and become suspended in the bulk fluid. In this case, the effective viscosity of a fluid with spherical rigid inclusions may be determined using a method proposed by Einstein.[112,113] Here, the extended form of Chong et al.[114] is preferred due to its applicability to a greater range of volume fractions. The relationship is given by:

$$\mu = \mu_0 \left(1 + \frac{[n]\varphi_m}{2} \left[\frac{\varphi/\varphi_m}{1-(\varphi/\varphi_m)} \right] \right)^2 \tag{60}$$

where φ is the volume fraction (degree of cure in this case), φ_m is the volume fraction at which the viscosity becomes infinite,[115] and $[n]$ is an intrinsic viscosity which is a measure of the effect of individual particles and is defined as:[115,116]

$$[n] = \lim_{\varphi \to 0} \frac{\left(\frac{\mu}{\mu_0} \right) - 1}{\varphi} \tag{61}$$

$[n]$ is 2.5 for rigid spheres but can range from 3-5 for angular particles.[116]

The third approach assumes that there is no appreciable transition zone between the fully cured and uncured material such that the cured material effectively reduces the width of channel (i.e. the crack opening) through which the healing agent can flow. This behaviour may be taken into account through a direct reduction of the crack width in the flow equation. An assessment of this third approach is made after the first two methods have been considered.

To calibrate the above viscosity relationships for CA, the experimental results of Gardner et al.[45] are considered. Gardner et al.[45] developed a custom-made viscometer to determine a time-viscosity relationship for CA. The viscometer consisted of a rectangular channel in a concrete specimen connected to transparent flexible tubes at each end, as illustrated in Figure 11. The flow of the healing agent through the viscometer was recorded using a high-speed video camera. The CA properties are given in Table 1.

Assuming that changes in flow rate can be described by an associated change in viscosity, the viscosities were calculated from a least-squares fit of the momentum balance equation to the experimentally measured flow rates.[43-45]
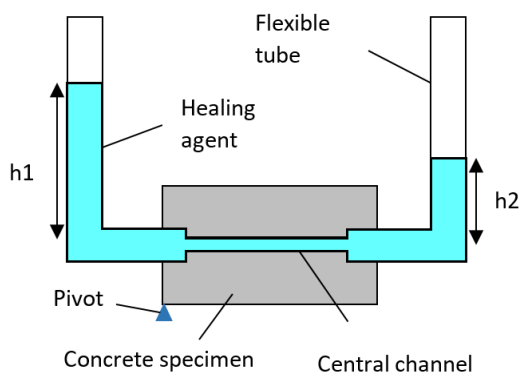

Figure 11 – Schematic of the custom viscometer of Gardner et al.[45]

The experimental results are compared with the corresponding model predictions in Figure 12. It can be seen from these data that the viscosity varies significantly throughout the course of the experiment. It was also observed that, after 2100 seconds, the flow of CA had ceased entirely.[45]
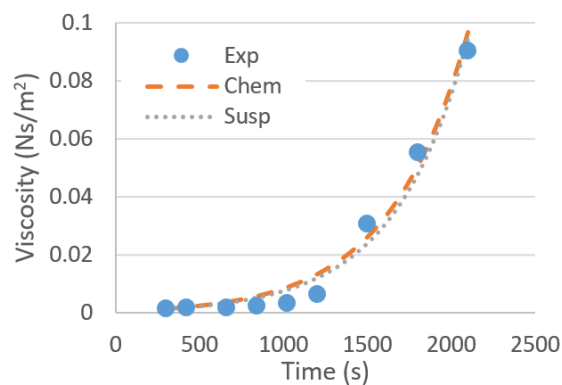

Figure 12 – Comparison of the viscosity model predictions with experimental data (using data from the unsaturated series of tests by Gardner et al.[45])

It may be seen from the Figure that both viscosity models are capable of reproducing the experimental behaviour with reasonable accuracy. The parameters used in the simulation are given in Table 5.

Table 5 – Curing and viscosity model parameters used in simulations

Parameter	Value	Parameter	Value
z_{c0} (mm)	1	$[n]$ (-)	2.5
τ (s)	2400	φ_m (-)	1
z_c (mm)	0	nv (-)	2.193
D (mm/mm²)	6	φ_g (-)	1

To assess the accuracy of the third approach, a computation was undertaken using the assumption that the change in flow rate results from a reduction in the crack width rather than a change in viscosity.

The crack widths were computed using a least-squares fit of the momentum balance equation to Gardner et al.'s flow data. A comparison between crack widths computed directly from the experimental data at selected time intervals and predicted crack widths using equation (51) -and the sharp curing-front curing assumption (denoted Cwr)- is given in Figure 13.

Under the sharp-front assumption, the crack width and the degree of cure are related as follows;

$$\varphi_{cwr} = 1 - \frac{w_{crk}}{w_{crk0}}$$

(62)

where φ_{cwr} is the degree of crack width reduction, w_{crk} is the calculated crack width and w_{crk0} is the original crack width.
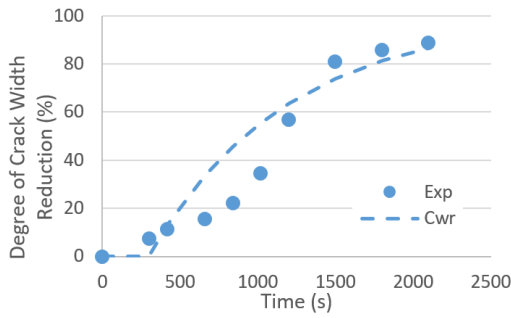

Figure 13 - Comparison of the crack width reduction predictions with experimental data with $z_{c0} = 0.5$ mm and $\tau = 900$ s

As can be seen from the figures, the match between the experimental data and numerical predictions is much better for the first two approaches than for the equivalent crack width reduction approach. The chemorheological model (equation 59) was selected for use in the full numerical model because it provides a good fit to the experimental data and accounts for the diffuse nature of the curing front.

Continuum flow and wall slip behaviour

The approach used to account for healing-agent curing in the (continuum) concrete matrix is based on the same chemorheological model. This predicts that, at a particular degree of cure (namely φ_g), the viscosity becomes infinite, at which point the healing agent has become a solid. In the matrix flow model component, this is taken into account in the effective diffusion coefficient (equation 8), which tends to zero as the viscosity tends to infinity.

In the discrete crack flow sub-model, the change in viscosity due to curing is taken into account through the viscous force term f (equation 2), which should become infinite as $\mu \to \infty$. However, this is not the case when the wall slip factor is included, since in this case f tends to the following expression:

$$f_{\mu \to \infty} = -\left(\frac{\mu}{k+0.5\mu w_{crk}\beta_w}\right)_{\mu \to \infty} u = -\left(\frac{1}{0.5 w_{crk}\beta_w}\right)u$$

(63)

The wall slip factor (β_w) in equation (63) depends on the properties of the crack face, including the roughness and the level of interfacial bonding. In the present case, the value of β_w should reduce as the degree of

interfacial bonding increases until, at full-cure, the wall slip should become zero (i.e. no slip occurs). To account for this, a relative wall slip factor (β_{wr}) is proposed, which is a function of the local degree of cure given by:

$$\beta_{wr} = 1 - \left(\frac{\varphi(x_c)}{\varphi_g}\right)^{nv} \tag{64}$$

where x_c denotes a position near the crack face and nv is the exponent taken from the chemorheological model.

Inserting this into the viscous force term results in the following expression that satisfies the limiting no-slip condition:

$$f_{\mu\to\infty} = -\left(\frac{\mu}{k+0.5\mu w_{crk}\beta_w\beta_{wr}}\right)_{\mu\to\infty} u = -\infty \tag{65}$$

6 Examples

Having presented the model theory and the implementation algorithm, along with a set of calibrations for the various model components, a series of examples are now presented, which were undertaken with the purpose of validating the full coupled model. These employ test data from the linked experimental programme of work.[99,117] The first example considers a test that measured the sorption of CA into a cracked concrete specimen; the second concerns the flow of CA within both a discrete natural concrete crack and a planar tapering crack, and the third considers a three-point bend test on a cementitious beam with embedded channels for delivering CA to cracked regions.

Table 6 – Parameters used in the simulations

Parameter	Value Example 1	Value Example 2a	Value Example 2b	Value Example 3
K_{int} (m^2)	3x10^{-17}	3x10^{-17}	3x10^{-21}	3x10^{-17}
n (-)	0.12	0.12	0.12	0.12
ρ_h (kg/m^3)	1060	1060	1060	1060
μ (Ns/m^2)	0.004	0.004	0.004	0.004
a (N/m^2)	1.86x10^7	1.86x10^7	1.86x10^7	1.86x10^7
m (-)	0.44	0.44	0.44	0.44
κ (-)	-3.0	-3.0	-3.0	-3.0
τ_m (s)	28.5	28.5	28.5	28.5
φ_g (-)	1	1	1	1
nv (-)	2.193	2.193	2.193	2.193
β_c/β_{crk} (s/m)	-	5x10^{-7}	5x10^{-8}	5x10^{-7}
z_{c0} (mm)	-	0.1	0.1	0.1
τ (s)	-	150	150	150
D (mm/mm^2)	-	5	5	5
z_c (mm)	-	1x10^{-5}	1x10^{-5}	1x10^{-5}
θ (rad)	-	0.17453	0.17453	0.17453
γ (N/m)	-	0.033	0.033	0.033
β_m (Ns/m^2)	-	0	0	0
β_s (-)	-	0	0	0
β_w (m^3/Ns)	-	0.003	0.01	0.003
c_1 (-)	-	1.325	1.325	1.325
c_2 (-)	-	0.35	0.35	0.35
w_{crit} (mm)	-	0.05	0.05	0.05

In all cases, the prismatic concrete specimens considered in these examples were cast, demoulded at 24 hours, cured under water for 5 days, dried in an oven for 1 day at 90 °C and then left in air for 1 day prior to testing.

The parameters used in the model for each of the examples can be seen in Table 6, and additional information on the mechanical model parameters is given in the Appendix.

The mesh(es) used for each example is shown in the relevant sub-section but all of these were chosen after mesh convergence studies. Similarly, the time steps used for the transient analyses, which were typically in the range 1 to 3s for a full model problem, were selected after time-step convergence checks. The mesh and time-step sizes were considered converged when the nodal variables changed by less than 1 %.

The value of the pore interaction factor (κ, in equation 9) was calibrated using experimental data from a set of concrete liquid permeability tests by Kameche et al.[118] The resulting comparison between the van Genuchten-Mualem relationship and Kameche et al.'s experimental results is given in Figure 14. It is noted that the negative value used for κ is consistent with the values given for concrete by Monlouis-Bonnaire et al.[119] and Poyet et al.[120]
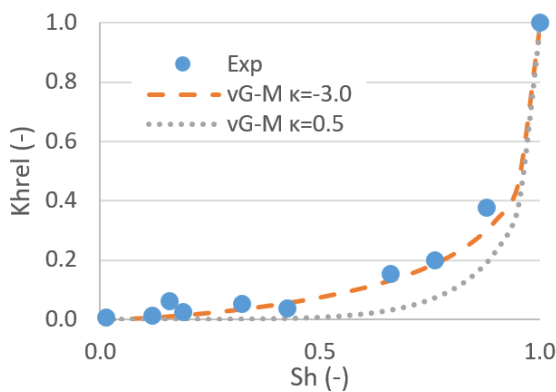

Figure 14 - Comparison of the permeability model predictions with experimental data

Example 1: Sorption.

The first example concerns the sorption of CA into a concrete sample through a crack surface.[99] In these experiments, the cured prisms (beams) were loaded to failure in three-point bending and then each half of the failed beam formed an individual specimen with a size of 127 x 75 x 75 mm. The sorption test involved placing the specimen, cracked side down, into a shallow bath of CA and capturing the sorption rise response using a high-speed camera. The test set up is illustrated in Figure 15. Two meshes were employed for the analysis, as illustrated in Figure 16.
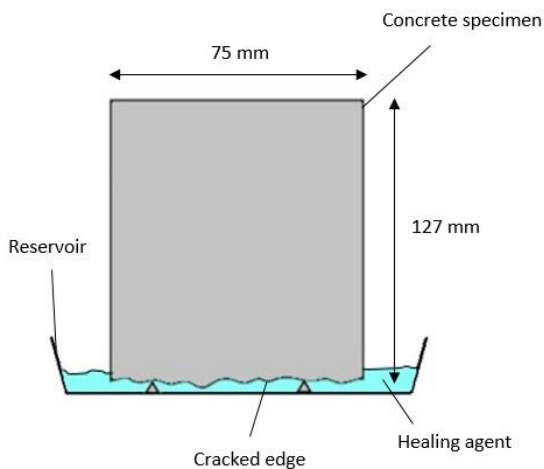

Figure 15 – Schematic of the absorption test set up of Selvarajoo et al.[99]
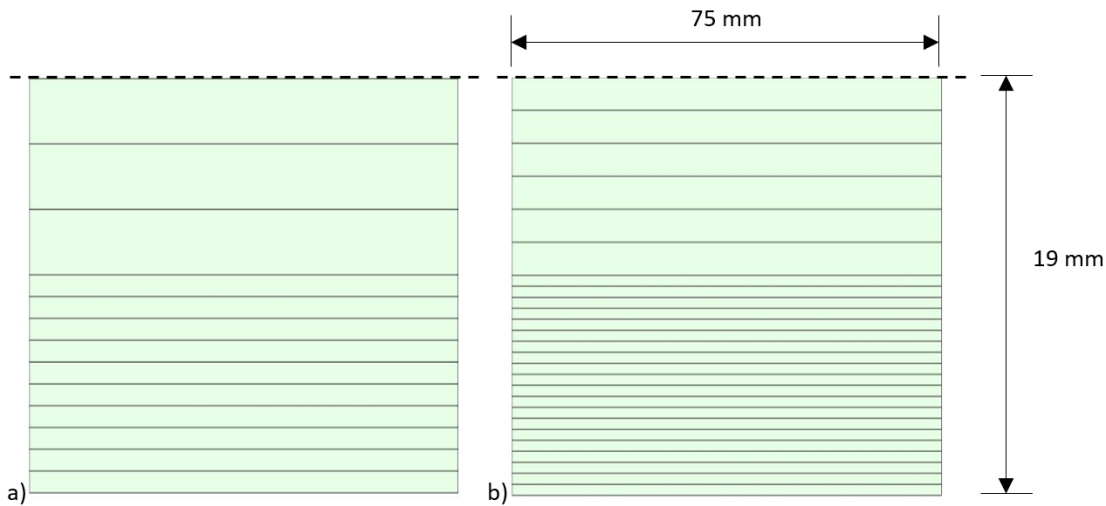
Figure 16 – Section of finite element meshes used for analysis a) Mesh1 and b) Mesh2

The experimental data were extracted from the video files based on the assumption that the mean capillary rise within the sample is that seen on the surface of the specimen, as illustrated in Figure 17c. These data are shown, along with the model predictions from both meshes, in Figures 17a & b. In may be seen that there is considerable scatter in the experimental data, which reflects the degree of variability of the sorption process in concrete. The simulations were based on the assumption that the observed rise height corresponded to a degree of saturation of 0.6, the value of which was chosen after a number of trial analyses and experimental saturation tests. The permeability coefficient was selected to reflect the fact that the concrete matrix adjacent to the crack face would have been micro-cracked since this zone was within the fracture process zone.[121]
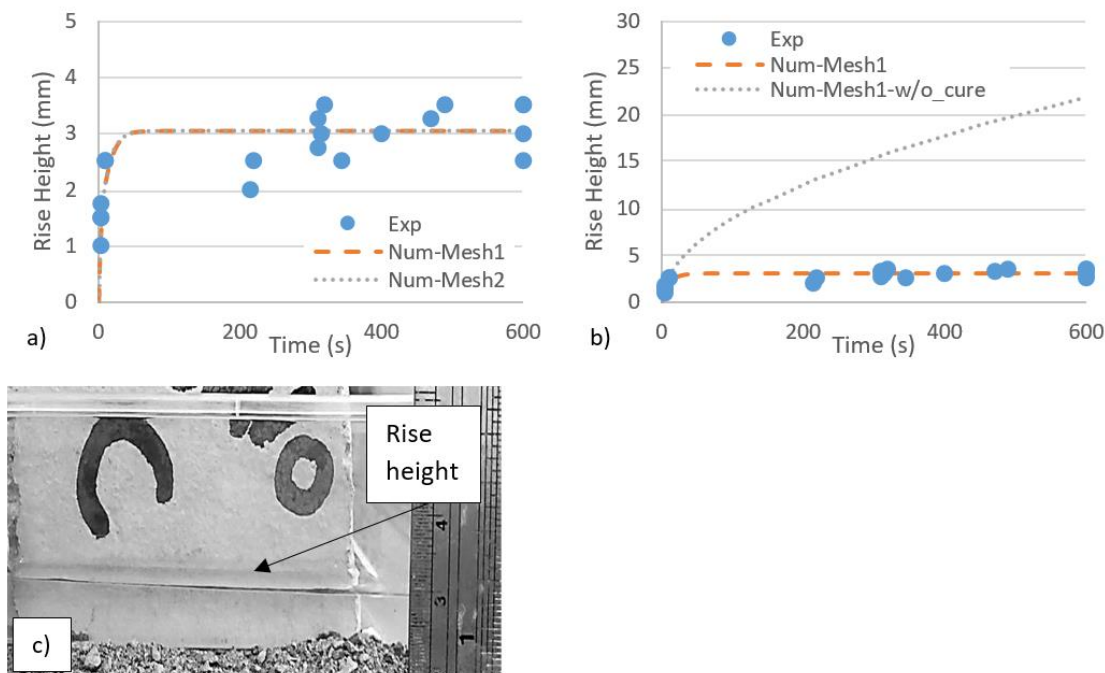

Figure 17 – Comparison of the rise height predictions a) with experimental data and b) with and without curing; c) rise height shown in test photograph

Notwithstanding the high variability of the experimental data, the comparison shows that the model is able to capture the characteristic sorption rise behaviour. A simulation in which healing-agent curing is not considered is also shown in Figure 17b. This shows the importance of simulating curing the present transport model.

Example 2: Flow through in a natural crack

The next example concerns the capillary rise of CA through a discrete natural concrete crack in unsaturated specimens.[99] The samples were prepared using essentially the same procedure as that described in example 1 except that the final tests specimens were cut from the centre of the cracked beam to a size of 90 x 75 x 25 mm and then clamped together with spacers to create crack widths of 0.1, 0.2 and 0.3 mm. The capillary rise test involved raising a reservoir of CA to the underside of the sample and then recording the fluid rise response with a high-speed camera. The test set up can be seen in Figure 18. The finite element meshes used for the analysis are shown in Figure 19.
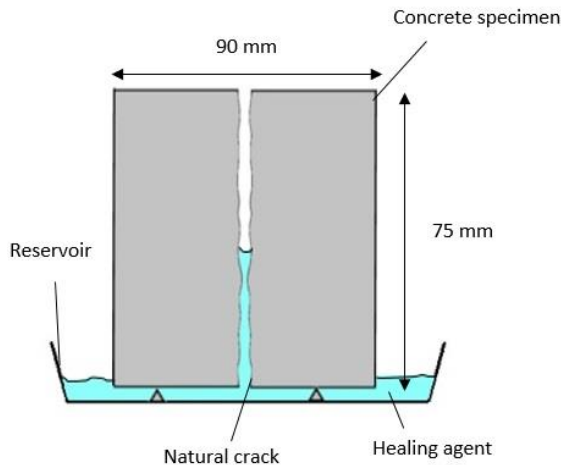

Figure 18 – Schematic of the natural crack flow test set up of Selvarajoo et al.[99]
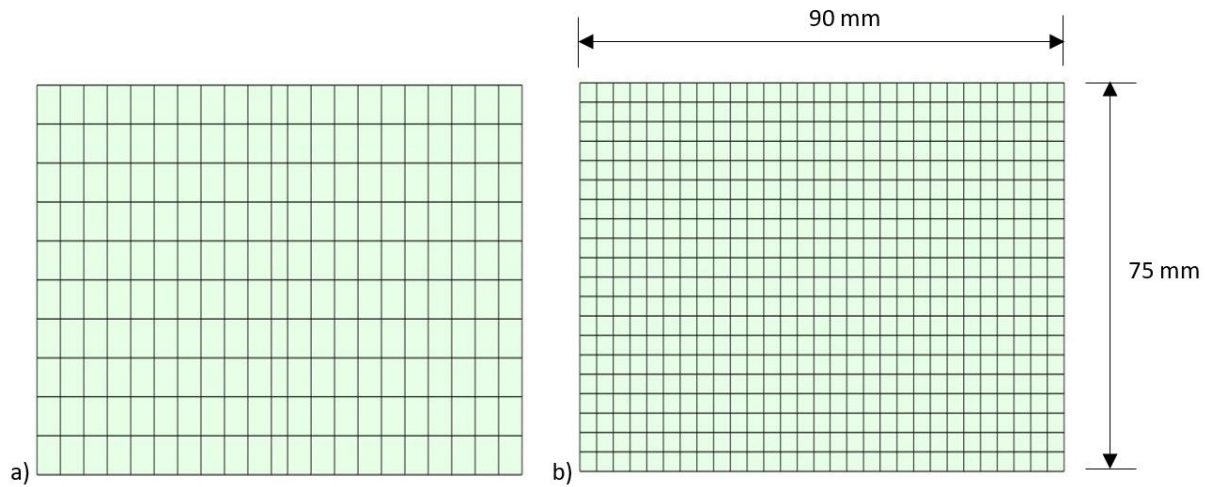

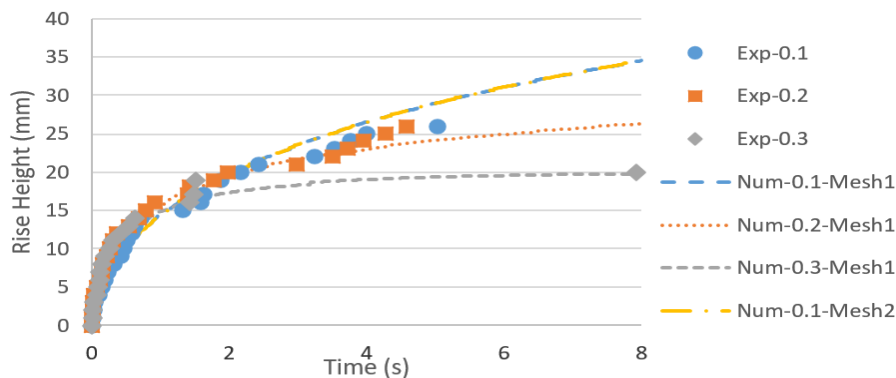Figure 19 – Finite element meshes used for analysis a) Mesh1 and b) Mesh2

Figure 20 – Comparison of the rise height predictions with experimental data

The results of the numerical simulation, along with the experimental data, are presented in Figure 20. It can be seen from the figure that the experimental data show similar rise height behaviour for all three crack widths, with the 0.1 mm and 0.2 mm results being particularly close to one another. This behaviour is significantly different from that observed in similar tests on planar (smooth surface) openings,[44] in which there were substantial differences between the flow response in channels with different openings (see below). The reason for this difference in behaviour between smooth-sided openings and natural cracks is believed to relate to the tortuous nature of natural cracks in which the actual flow path may be considerably greater than the recorded rise height. Furthermore, in cracks with rough surfaces, the crack opening varies considerably from the mean and cured CA may block the narrowest sections of the opening long before all flow ceases. Despite the above complexities, the figure shows that the numerical model is able of capturing the capillary rise behaviour reasonably well although it is acknowledged that local crack tortuosity effects are not explicitly simulated.

For completeness, the results from a series of simulations that considered the aforementioned tests on planar tapered openings are presented here.[44] The test set up and finite element meshes used for the analyses were the same as in the previous example.
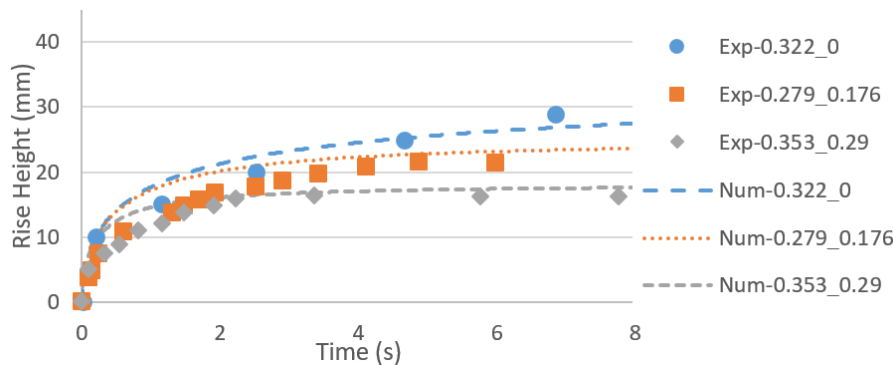

Figure 21– Comparison of the rise height predictions with experimental data

The results of the numerical simulation along with the experimental data are given in Figure 21. It can be seen from the figure that the experimental data in this case shows a greater difference in rise height behaviour for each of the crack widths, and that the numerical simulation is able to accurately capture this behaviour.

Example 3: Three-point bend test on a beam with embedded channels

The final example considers a series of tests on notched concrete beam specimens (255 x 75 x 75 mm) with embedded channels that were loaded in three-point bending,[117] as illustrated in Figure 22. The channels were connected to flexible tubes at either side of the specimen and then filled with CA. One of the ends was then clamped, whilst the other was attached to a pressure regulator and an airline. The specimens were then tested in three-point bending under different loading rates and under different applied pressures (namely 1.0, 0.5, 0.3, 0.1 and 0.0 bar). In the present study, the tests corresponding to a loading rate of 0.001 mm/s were simulated.
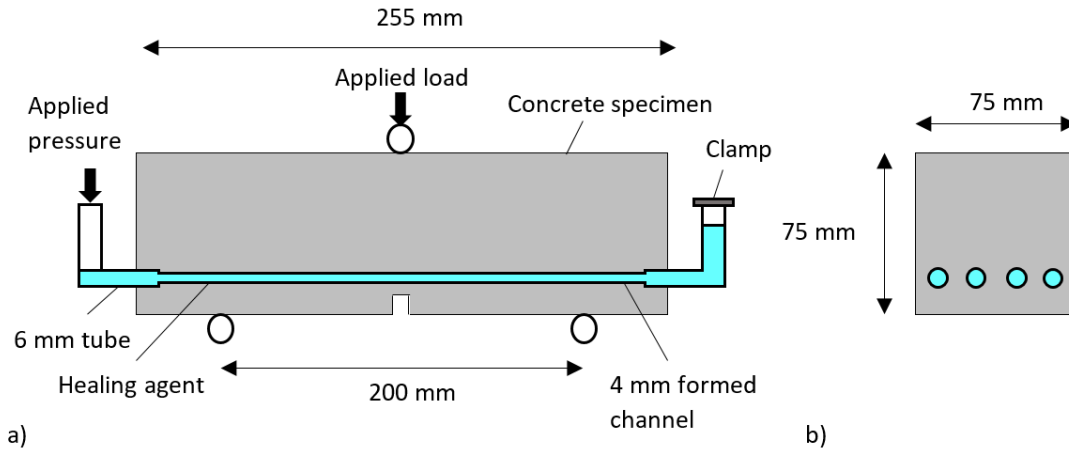
Figure 22 – Schematic of the three-point bending test set up of Selvarajoo et al.[117] a) elevation and b) cross-section
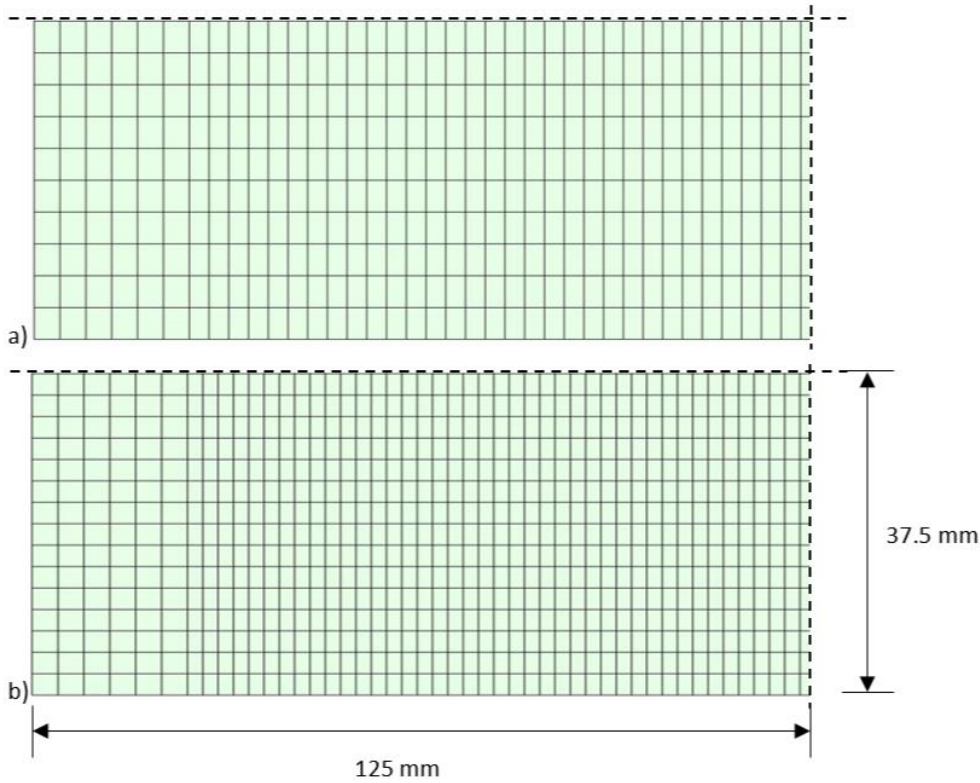
Figure 23 – Section of finite element meshes used for analysis a) Mesh1 and b) Mesh2

A section of the two finite element meshes, used for the analysis can be seen in Figure 23.

Experimental observations suggest that the minimum size of the opening that the healing agent could flow through depended on the applied pressure.[117] In the present work, the minimum crack width which the flow can enter is dealt with using an empirical function of the applied pressure and is given here as:

$$w_{cmin} = AP_{app} + B \tag{66}$$

The proposed function (applicable in the range $1bar \geq P_{app} \geq 0$) is consistent with the experimental data. In the present work, the constants are given as $A = -0.05$ mm/bar and $B = 0.095$ mm.

Figure 24 – Comparison of the rise height predictions a) with experimental data and b) with different mesh sizes
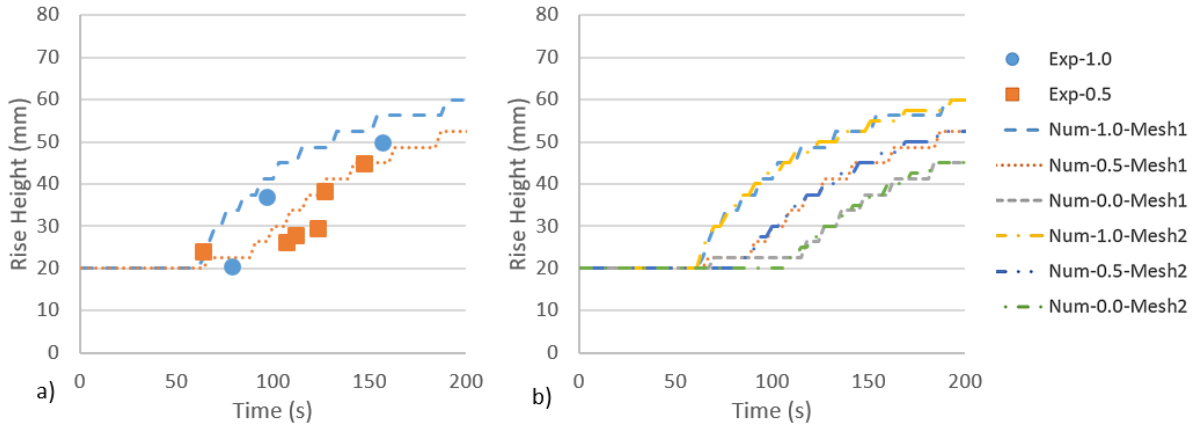
The experimental data is limited in this case and only relates to the extent of healing agent visible on the side of the test beam. Nevertheless, a comparison between these data and the 2D numerical predictions is given in Figure 24. The resulting comparison between this limited experimental data and the numerical model is considered to provide a partial validation of the coupled flow model.

The stepped nature of the numerical responses shown in Figure 24 relate to the fact that the flow is much faster than the cracking; thus, the crack widths increase with loading until, ahead of the flow front, the crack width becomes greater than w_{cmin}, and the flow advances.
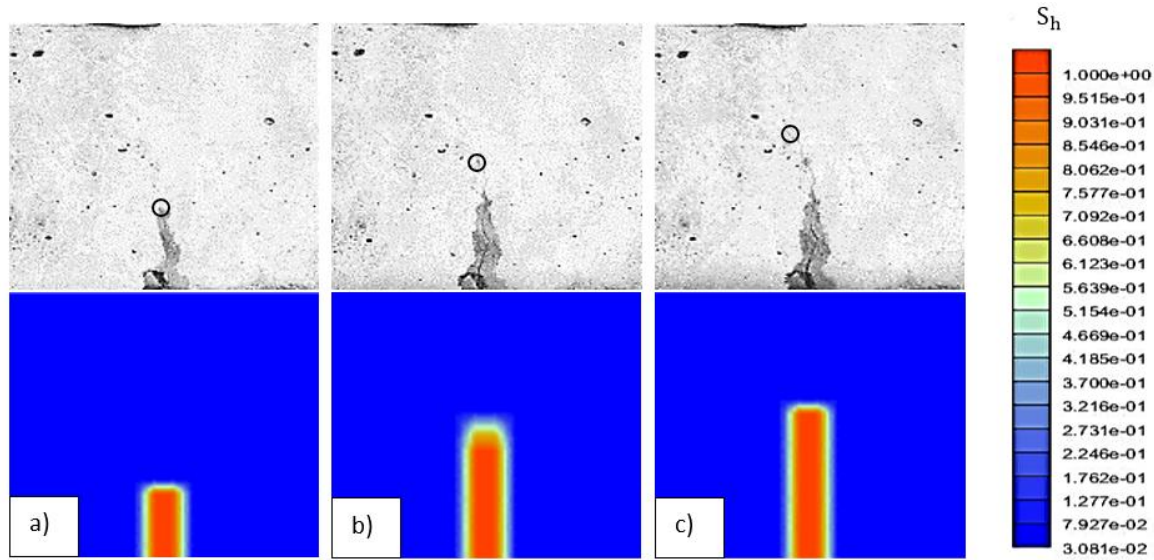

Figure 25 – Comparison of predicted saturation contour compared with experimental data for the case corresponding to an applied pressure of $P_{app} = 0.5\ bar$ at a) $t = 85\ s$ b) $t = 127\ s$ and c) $t = 147\ s$, the black circles indicate the position of the flow front in the crack

A comparison between the saturation contours predicted by the model and pictures taken from recordings of the experiment can be seen in Figure 25; whilst a deformed mesh plot showing the healing agent in the crack and the degree of cure can be seen in Figure 26. A deformed contour plot showing the degree of cure in the crack and in the concrete matrix can be seen in Figure 27. Figure 25 shows that the numerical model provides a reasonable prediction of the saturation of the specimen. The deformed contour shown in Figure 26 shows that by the end of the test, the crack tip has almost reached the top of the beam, and that the adhesive fills most of the crack.

The average degree of cure (φ_{av}) of the healing agent at any position (height) within a crack is determined from the curing-front model by integrating the degree of cure across the crack opening (Section 5). In general, φ_{av} depends on the curing time, which is measured from when the fluid is first in contact with the substrate

(crack wall), and the transient crack opening. A plot of φ_{av} values in the crack at three different times is shown in Figure 26. As expected, φ_{av} is least at the flow front, where the glue has not yet had time to cure, and is also less for wider cracks, since the greater the crack opening, the greater the time required for the curing front to propagate across the body of fluid. At the final time shown, the maximum value is 23.06 %. Figure 27 shows φ_{av} for both the crack and the surrounding matrix and it is apparent that the degree of cure is much higher in the matrix, with a maximum value of 99.44 %, than in the crack. This is again as expected since the size of the pores is much smaller than that of the crack opening.
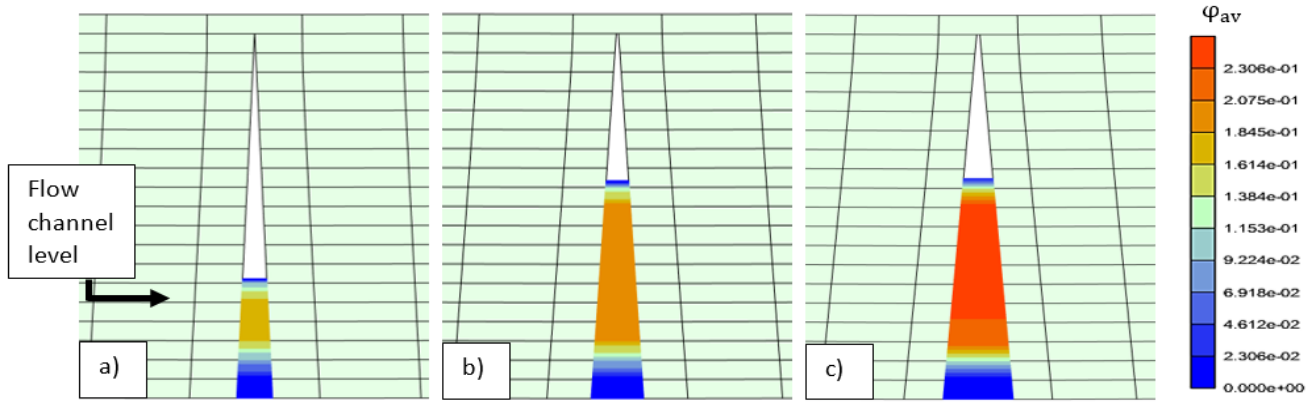

Figure 26 – Deformed mesh plot showing the healing agent in the crack and the degree of cure for the case corresponding to an applied pressure of $P_{app} = 0.5\ bar$ at a) $t = 85\ s$ b) $t = 127\ s$ and c) $t = 147\ s$
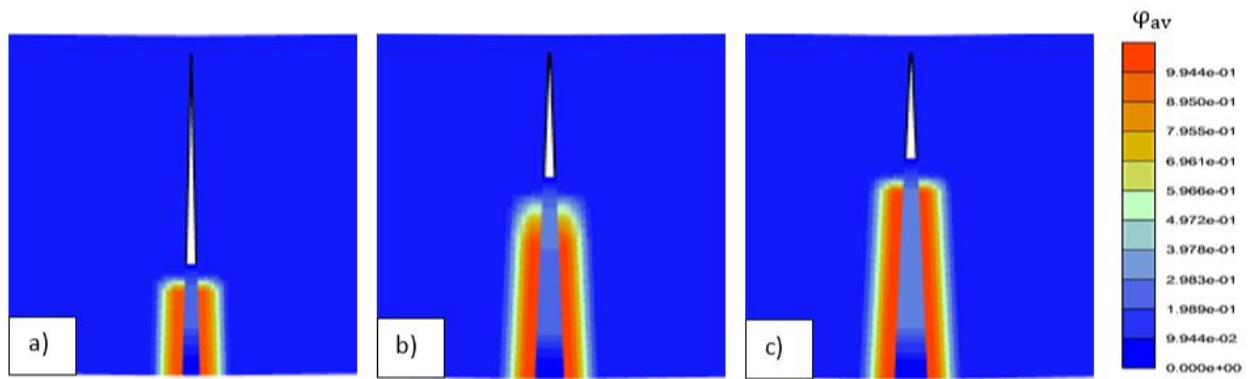

Figure 27 – Deformed contour plot showing the degree of cure in the crack and the concrete matrix for the case corresponding to an applied pressure of $P_{app} = 0.5\ bar$ at a) $t = 85\ s$ b) $t = 127\ s$ and c) $t = 147\ s$

7 Discussion

The coupled model presented in this study is based on experimental observations of the underlying physical processes that govern SH systems with embedded channels. Such SH systems are complex and are governed by a number of interacting processes, which are simulated using an associated set of tractable sub-models. Each of these sub-models requires a limited number of physically meaningful parameters that can either be determined directly using the type of test described in this paper, which might not be practicable in many situations, or obtained from product data (e.g. glue material data sheets), with guidance from the values given in this article. Although any one sub-model requires a limited number of parameters, it is acknowledged that the aggregated set of parameters is relatively large (i.e. 23 parameters are given in Table 6).

The results of the sensitivity studies presented in this paper (i.e. on the effect of inertia, DCA and healing agent curing), as well as the overall comparisons with experimental responses, suggest that neglecting any of these processes can lead to a significant difference in the predicted behaviour. This leads the authors to conclude that it is necessary to consider all of the identified physical processes in the model.

Although the complexity of the combined coupled model might suggest that it is computationally expensive, in 3D, it only has three main transport variables and three mechanical variables (i.e. displacement components), which is similar to many of the coupled models reviewed in the introductory section of this paper. This, combined with the experience the authors have gained with the model to date, suggests that it would be viable for simulating full-scale structural self-healing systems.

8 Conclusions

In this study, a new coupled computational model for simulating the reactive discrete-continuum flow of a healing agent in cementitious materials was described. The following conclusions can be drawn from the work:

- The proposed coupled computational model is capable of simulating the reactive flow of a healing agent in cementitious materials, including unsaturated matrix flow and flow through discrete cracks.
- The addition of a jump penalty on the pressure gradient across element edges is an effective approach for stabilising transient discrete crack flow simulations.
- Spurious oscillations in the unsaturated continuum matrix flow computations can be effectively damped using a higher order mass matrix approach.
- The meniscus dynamic contact angle behaviour is well-represented using the relationship proposed by Jiang et al.[97] with the parameters computed using experimental data from an associated experimental study.[99]
- The new approach for modelling the effects of CA curing within discrete concrete cracks, using a diffuse curing front model, is able to accurately reproduce experimental observed curing behaviour for a range of crack openings.
- The transient variation of CA viscosity, in both continuum and discrete-crack flows, is well-represented by the chemorheological model of Castro and Macosko.[109]
- The effects of curing on the wall-slip behaviour of CA flow in a discrete crack may be simulated with a new relationship that accounts for the gradual reduction in slip potential with the increasing degree of cure.
- The proposed coupled finite element model is able to represent the characteristic continuum and discrete flow of a cementitious vascular self-healing system, as demonstrated with a series of validation examples.

Appendix

The constitutive relationship for the damage-healing model relates the stress to the relative displacements across the crack band and is expressed as (for a single phase of healing):

$$\sigma = (1 - \omega)Ku + \omega h(1 - \omega_h)K(u - u_h) \tag{67}$$

where $K = E/w_b$ is the stiffness of the crack band (E denotes Young's modulus and w_b the width of the crack band), ω is the damage variable which ranges from 0 for no damage to 1 for full damage, h is the degree of healing, u_h is the relative displacement at which healing takes place and ω_h is the damage variable for the healing material.

The damage evolution functions depend on the maximum values of the inelastic relative displacements, ζ and ζ_h, and are given as:

$$\omega(\zeta) = 1 - \frac{f_t}{K\zeta} e^{\frac{-c\zeta}{\zeta_m}} \qquad \omega_h(\zeta_h) = 1 - \frac{f_{th}}{K\zeta_h} e^{\frac{-c\zeta_h}{\zeta_{mh}}} \tag{68}$$

where f_t and f_{th} are the tensile strengths of the virgin and healed material, $c = 5$ is a softening constant and ζ_m and ζ_{mh} are the effective relative displacements at the end of the softening curve for the virgin and healed material respectively.

The mechanical damage-healing model parameters can be seen in Table 7.

Table 7 – Mechanical damage-healing parameters

Parameter	Value	Parameter	Value
f_t (N/mm^2)	2.1-3.0	E (N/mm^2)	30000
ζ_m (mm)	0.13-0.15	ν (-)	0.2
f_{th} (N/mm^2)	3.0	w_b (mm)	4
ζ_{mh} (mm)	0.2		

Acknowledgements

References

1   Baroghel-Bouny V, Nguyen TQ, Dangla P. Assessment and prediction of RC structure service life by means of durability indicators and physical/chemical models. Cement and Concrete Composites. 2009;31(8):522–534. doi:10.1016/j.cemconcomp.2009.01.009.

2   Gawin D, Pesavento F, Schrefler BA. Modeling deterioration of cementitious materials exposed to calcium leaching in non-isothermal conditions. Computer Methods in Applied Mechanics and Engineering. 2009;198(37–40):3051–3083. doi:10.1016/j.cma.2009.05.005.

3   Grymin W, Gawin D, Koniorczyk M, Pesavento F. Experimental and numerical investigation of the alkali-silica reaction in the cement-based materials. Archives of Civil and Mechanical Engineering. 2018;18(4):1698–1714.doi:10.1016/j.acme.2018.07.003.

4   Gardner D, Lark R, Jefferson AD, Davies R. A survey on problems encountered in current concrete construction and the potential benefits of self-healing cementitious materials. Case Studies in Construction Materials. 2018;8:238-247

5   Van Tittelboom K, De Belie N. Self-healing in cementitious materials-a review. Materials. 2013;6(6):2182-2217

6   De Belie N, Gruyaert E, Al-Tabbaa A, Antonaci P, Baera C, Darquennes A, Davies R, Ferrara L, Jefferson T, Litina C, Miljevic B, Otlewska A, Ranogajec J, Roig-Flores M, Paine K, Lukowski P, Serna P, Tulliani JM, Vucetic S, Wang J, Jonkers HM. A review of self-healing concrete for damage management of structures. Advanced Materials Interfaces. 2018;1800074:1–28.

7   Kanellopoulos A, Giannaros P, Palmer D, Kerr A, Al-Tabbaa A. Polymeric microcapsules with switchable mechanical properties for self-healing concrete: Synthesis, characterisation and proof of concept. Smart Materials and Structures. 2017;26(4). doi:10.1088/1361-665X/aa516c.

8   Souza L, Al-Tabbaa A. Microfluidic fabrication of microcapsules tailored for self-healing in cementitious materials. Construction and Building Materials. 2018;184:713–722. doi:10.1016/j.conbuildmat.2018.07.005.

9   Formia A, Irico S, Bertola F, Canonico F, Antonaci P, Pugno NM, Tulliani JM. Experimental analysis of self-healing cement-based materials incorporating extruded cementitious hollow tubes. Journal of Intelligent Material Systems and Structures. 2016;27(19):2633–2652. doi:10.1177/1045389X16635847.

10   Van Tittelboom K, Wang J, Araújo M, Snoeck D, Gruyaert E, Debbaut B, Derluyn H, Cnuddle V, Tsangouri E, Van Hemelrijck D, De Belie N. Comparison of different approaches for self-healing concrete in a large-scale lab test. Construction and Building Materials. 2016;107:125–137. doi:10.1016/j.conbuildmat.2015.12.186.

11   Joseph C, Jefferson AD, Isaacs B, Lark R, Gardner D. Experimental investigation of adhesive-based self-healing of cementitious materials. Magazine of Concrete Research. 2010;62(11):831–843.

12   Minnebo P, Thierens G, De Valck G, Van Tittelboom K, De Belie N, Van Hemelrijck D, Tsangouri E. A novel design of autonomously healed concrete: Towards a vascular healing network. Materials. 2017;10(1):1–23. doi:10.3390/ma10010049.

13   Jonkers H, Thijssen A, Muyzer G, Copuroglu O, Schlangen E. Application of bacteria as self-healing agent for the development of sustainable concrete. Ecological Engineering. 2010;36(2):230-235

14   Wang J, Van Tittelboom K, De Belie N, Verstraete W. Use of silica gel or polyurethane immobilized bacteria for self-healing concrete. Construction and Building Materials. 2012;26(1):532-540

15   Dry C. Matrix cracking repair and filling using active and passive modes for smart timed release of chemicals from fibers into cement matrices. Smart Materials and Structures. 1994;3(2):118–123.

16   Ferrara L, Van Mullem T, Alonso MC, Antonaci P, Borg RP, Cuenca E, Jefferson T, NG PL, Peled A, Roig-Flores M, Sanchez M, Schroefl C, Serna P, Snoeck D, Tulliani JM, De Belie N. Experimental characterization of the self-healing capacity of cement based materials and its effects on the material performance: A state of the art report by COST Action SARCOS WG2. Construction and Building Materials. 2018;167:115–142. doi:10.1016/j.conbuildmat.2018.01.143.

17   Sidiq A, Gravina R, Giustozzi F. Is concrete healing really efficient? A review. Construction and Building Materials. 2019;205:257-273

18   Xue C, Li W, Li J, Tam VWY, Ye G. A review study on encapsulation-based self-healing for cementitious materials, Structural Concrete. 2019;20:198-212

19   Schimmel EC, Remmers J. Development of a constitutive model for self-healing materials. Delft Aerospace Computational Science, Report DACS-06-003 2006

20   Remmers J, de Borst R. Numerical modelling of self-healing mechanisms. In. Self Healing Materials. Springer 2008; 365-380

21   Abu Al-Rub R, Darabi MK, Little DN, Masad EA. A micro-damage healing model that improves prediction of fatigue life in asphalt mixes. International Journal of Engineering Science. 2010;48(12):966-990

22   Huang H, Ye G. Simulation of self-healing by further hydration in cementitious materials. Cement and Concrete Composites. 2012;34(4):460-467

23   Mergheim J, Steinmann P. Phenomenological modelling of self-healing polymers based on integrated healing agents. Computational Mechanics. 2013;52(3):681–692. doi:10.1007/s00466-013-0840-0.

24   Zemskov S, Jonkers H, Vermolen F. A mathematical model for bacterial self-healing of cracks in concrete. Journal of Intelligent Material Systems and Structures. 2014;25(1):4-12

25   Davies R, Jefferson AD. Micromechanical modelling of self-healing cementitious materials. International Journal of Solids and Structures. 2017;113–114:180–191. doi:10.1016/j.ijsolstr.2017.02.008.

26   Di Luzio G, Ferrara L, Krelani V. Numerical modeling of mechanical regain due to self-healing in cement based composites. Cement and Concrete Composites. 2018;86:190–205. doi:10.1016/j.cemconcomp.2017.11.006.

27   Jefferson T, Javierre E, Freeman B, Zaoui A, Koenders E, Ferrara L. Research progress on numerical models for self-healing cementitious materials. Advanced Materials Interfaces. 2018:1–19. doi:10.1002/admi.201701378.

28   Algaifi HA, Bakar AB, Sam ARM, Abidin ARZ, Shahir S, Al-Towayti WAH. Numerical modeling for crack self-healing concrete by microbial calcium carbonate. Construction and Building Materials. 2018;189:816-824

29   Mauludin LM, Zhuang X, Rabczuk T. Computational modeling of fracture in encapsulation-based self-healing concrete using cohesive elements. Composite Structures. 2018;196:63-75

30   Oucif C, Voyiadjis GZ, Kattan PI, Rabczuk T. Nonlinear superhealing and contribution to the design of a new strengthening theory. Journal of Engineering Mechanics. 2018;144(7)

31   Oucif C, Voyiadjis GZ, Rabczuk T. Modeling of damage-healing and nonlinear self-healing concrete behaviour: application to coupled and uncoupled self-healing mechanisms. Theoretical and Applied Fracture Mechanics. 2018;96:216-230

32   Ponnusami SA, Krishnasamy J, Turteltaub S, van der Zwaag S. A cohesive-zone crack healing model for self-healing materials. International Journal of Solids and Structures. 2018;134:249-263

33   Shahsavari H, Baghani M, Naghdabadi R, Sohrabpour S. A thermodynamically consistent viscoelastic-viscoplastic constitutive model for self-healing materials. Journal of Intelligent Material Systems and Structures. 2018;29(6):1065-1080

34   Voyiadjis GZ, Kattan PI. Decomposition of healing tensor: in continuum damage and healing mechanics. International Journal of Damage Mechanics. 2018;27(7):1020-1057

35   Zhang Y, Zhuang X. A softening-healing law for self-healing quasi-brittle materials: analysing with strong discontinuity embedded approach. Engineering Fracture Mechanics. 2018;192:290-306

36   Sanz-Herrera JA, Aliko-Benitez A, Fadrique-Contreras AM. Numerical investigation of the coupled mechanical behaviour of self-healing materials under cyclic loading. International Journal of Solids and Structures. 2019;160:232-246.

37   Darabi MK, Abu Al-Rub A, Little DN. A continuum damage mechanics framework for modeling micro-damage healing. International Journal of Solids and Structures. 2012;49(3-4):492-513

38   Papadakis V, Vayenas C, Fardis M. A reaction engineering approach to the problem of concrete carbonation. AIChE Journal. 1989;35(10):1639-1650

39   Saetta AV, Schrefler BA, Vitaliani RV. 2-D model for carbonation and moisture/heat flow in porous materials. Cement and Concrete Research. 1995;25(8):1703-1712

40   Koenders EAB. Modelling the self healing potential of dissoluble encapsulated cement systems. 2012

41   Aliko-Benitez A, Doblare M, Sanz-Herrera JA. Chemical-diffusive modeling of the self-healing behaviour in concrete. International Journal of Solids and Structures. 2015;69-70:392-402

42   Chitez AS, Jefferson AD. A coupled thermo-hygro-chemical model for characterising autogenous healing in ordinary cementitious materials. Cement and Concrete Research. 2016;88:184–197. doi:10.1016/j.cemconres.2016.07.002.

43   Gardner D, Jefferson AD, Hoffman A. Investigation of capillary flow in discrete cracks in cementitious materials. Cement and Concrete Research. 2012;42(7):972–981. doi:10.1016/j.cemconres.2012.03.017.

44   Gardner D, Jefferson AD, Hoffman A, Lark R. Simulation of the capillary flow of an autonomic healing agent in discrete cracks in cementitious materials. Cement and Concrete Research. 2014;58:35–44. doi:10.1016/j.cemconres.2014.01.005.

45   Gardner D, Herbert D, Jayaprakash M, Jefferson AD, Paul A. Capillary flow characteristics of an autogenic and autonomic healing agent for self-healing concrete. Journal of Materials in Civil Engineering. 2017;29(11):4017228. doi:10.1061/(ASCE)MT.1943-5533.0002092.

46   Gilabert FA, Van Tittelboom K, Van Stappen J, Cnuddle V, De Belie N, Van Paepegem W, Integral procedure to assess crack filling and mechanical contribution of polymer-based healing-agent in encapsulation-based self-healing concrete. Cement and Concrete Composites. 2017;77:68-80

47   Jasak H. OpenFOAM: open source cfd in research and industry. International Journal of Naval Architecture and Ocean Engineering. 2009;1(2):89-94

48   Suzuki A, Fomin S, Chugunov V, Hashida T. Mathematical modeling of non-Fickian diffusional mass exchange of radioactive contaminants in geological disposal formations. Water (Switzerland). 2018; 0(2):1–11. doi:10.3390/w10020123.

49   Lecampion B, Bunger A, Zhang X. Numerical methods for hydraulic fracture propagation: A review of recent trends. Journal of Natural Gas Science and Engineering. 2018;49(October 2017):66–83. doi:10.1016/j.jngse.2017.10.012.

50   Roels S, Vandersteen K, Carmeliet J. Measuring and simulating moisture uptake in a fractured porous medium. Advances in Water Resources. 2003;26(3):237–246. doi:10.1016/S0309-1708(02)00185-9.

51   Roels S, Moonen P, De Proft K, Carmeliet J. A coupled discrete-continuum approach to simulate moisture effects on damage processes in porous materials. Computer Methods in Applied Mechanics and Engineering. 2006;195(52):7139–7153.

52   Carmeliet J, Delerue JF, Vandersteen K, Roels S. Three-dimensional liquid transport in concrete cracks. International Journal for Numerical and Analytical Methods in Geomechanics. 2004; 8(7–8):671–687. doi:10.1002/nag.373.

53   Soltani M, Chen P. Numerical Modeling of interstitial fluid flow coupled with blood flow through a remodeled solid tumor microvascular network. PLoS ONE. 2013;8(6). doi:10.1371/journal.pone.0067025.

54   Troendle EP, Khan A, Searson PC, Ulmschneider MB. Predicting drug delivery efficiency into tumor tissues through molecular simulation of transport in complex vascular networks. Journal of Controlled Release. 2018;292:221-234

55   Howard G, Fast C. Optimum fluid characteristics for fracture extension. Drilling and Production Practices. 1957;261-270

56   de Borst R. Fluid flow in fractured and fracturing porous media: A unified view. Mechanics Research Communications. 2017;80:47–57. doi:10.1016/j.mechrescom.2016.05.004.

57   Cao TD, Hussain F, Schrefler BA. Porous media fracturing dynamics: stepwise crack advancement and fluid pressure oscillations. Journal of the Mechanics and Physics of Solids. 2018;111:113–133. doi:10.1016/j.jmps.2017.10.014.

58   Lecampion B, Garagash DI. Confined flow of suspensions modelled by a frictional rheology. Journal of Fluid Mechanics. 2014;759:197–235. doi:10.1017/jfm.2014.557.

59   Bao K, Lavrov A, Nilsen HM. Numerical modeling of non-Newtonian fluid flow in fractures and porous media. Computational Geosciences. 2017;21(5–6):1313–1324. doi:10.1007/s10596-017-9639-y.

60   Milanese E, Yilmaz O, Molinari JF, Schrefler BA. Avalanches in dry and saturated disordered media at fracture in shear and mixed mode scenarios. Mechanics Research Communications. 2017;80:58-68

61   Pizzocolo F, Huyghe JM, Ito K. Mode I crack propogation in hydrogels is step wise. Engineering Fracture Mechanics. 2013;97:72-79

62   Réthoré J, de Borst R, Abellan MA. A two-scale approach for fluid flow in fractured porous media. International Journal for Numerical Methods in Engineering. 2007;71:780-800. doi:10.1002/nme.1962.

63   Réthoré J, de Borst R, Abellan MA. A two-scale model for fluid flow in an unsaturated porous medium with cohesive cracks. Computational Mechanics. 2008;42(2):227–238. doi:10.1007/s00466-007-0178-6.

64   Mourik S, Veldman a. EP, Dreyer ME. Simulation of capillary flow with a dynamic contact angle. Microgravity - Science and Technology. 2005;17(3):87–93. doi:10.1007/BF02872093.

65   Dujc A, Brank B, Ibrahimbegovic A. Stress-hybrid quadrilateral finite element with embedded strong discontinuity for failure analysis of plane stress solids. International Journal for Numerical Methods in Engineering. 2013;94:1075-1098

66   Alfaiate J, Simone A, Sluys LJ. Non-homogeneous displacement jumps in strong embedded discontinuities. International Journal of Solids and Structures. 2003;40(21):5799–5817. doi:10.1016/S0020-7683(03)00372-X.

67   Alfaiate J, Wells GN, Sluys LJ. On the use of embedded discontinuity elements with crack path continuity for mode-I and mixed-mode fracture. Engineering Fracture Mechanics. 2002;69(6):661–686. doi:10.1016/S0013-7944(01)00108-4.

68   Smith NP, Pullan AJ, Hunter PJ. An Anatomically Based Model of Transient Coronary Blood Flow in the Heart. SIAM Journal on Applied Mathematics. 2002;62(3):990–1018.

69   Pontrelli G, Rossoni E. Numerical modelling of the pressure wave propagation in the arterial flow. International Journal for Numerical Methods in Fluids. 2003;671(March 2002):651–671.

70   Milišić V, Quarteroni A. Analysis of lumped parameter models for blood flow simulations and their relation with 1D models. ESAIM: Mathematical Modelling and Numerical Analysis. 2004;38(4):613–632. doi:10.1051/m2an:2004036.

71   Mooney M. Explicit Formulas for Slip and Fluidity. Journal of Rheology. 1931;2(2):210–222. doi:10.1122/1.2116364.

72   Lee SH, Lough M, Jensen C. Hierarchical modeling of flow in naturally fractured formations with multiple length scales. Water Resources Research. 2001;37(3):443-455

73   Li L, Lee SH. Efficient field-scale simulation of black oil in a naturally fractured reservoir through discrete fracture networks and homogenized media. SPE Reservoir Evaluations and Engineering. 2008;11(4):750-758

74   Hajibeygi H, Karvounis D, Jenny P. A hierarchical fracture model for the iterative multiscale finite volume method. Journal of Computational Physics. 2011;230(24):8729-8743

75   Xu J, Sun B, Chen B. A hybrid embedded discrete fracture model for simulating tight porous media with complex fracture systems. Journal of Petroleum Science and Engineering. 2019;174:131-143

76   Alfaiate J, Moonen P, Sluys LJ, Carmeliet J. On the use of strong discontinuity formulations for the modeling of preferential moisture uptake in fractured porous media. Computer Methods in Applied Mechanics and Engineering. 2010;199(45–48):2828–2839. doi:10.1016/j.cma.2010.05.004.

77   Hamraoui A, Nylander T. Analytical approach for the Lucas-Washburn equation. Journal of Colloid and Interface Science. 2002;250(2):415–421. doi:10.1006/jcis.2002.8288.

78   Schäffer E, Wong PZ. Dynamics of contact line pinning in capillary rise and fall. Physical Review Letters. 1998;80(14):3069–3072. doi:10.1103/PhysRevLett.80.3069.

79   Burman E, Fernandez M, Hansbo P. Continuous interior penalty finite element method for oseen's equations. SIAM Journal on Numerical Analysis. 2006;44(3):1248-1274

80   Claus S, Kerfriden P. A cutfem method for two-phase flow problems. Computer Methods in Applied Mechanics and Engineering. 2019;348:185-206

81   Gawin D, Pesavento F, Schrefler BA. Hygro-thermo-chemo-mechanical modelling of concrete at early ages and beyond. Part I: hydration and hygro-thermal phenomena. International Journal for Numerical Methods in Engineering. 2006;67(3):299–331. doi:10.1002/nme.1615.

82   Davie CT, Pearce CJ, Kukla K, Bićanić N. Modelling of transport processes in concrete exposed to elevated temperatures – An alternative formulation for sorption isotherms. Cement and Concrete Research. 2018;106(August 2016):144–154. doi:10.1016/j.cemconres.2018.01.012.

83   Mualem Y. A new model for predicting the hydraulic conductivity of unsaturated porous media. Water Resources Research. 1976;12(3):513-522

84   van Genuchten MT. A closed-form equation for predicting the hydraulic conductivity of unsaturated soils. Soil Science Society of America Journal. 1980;44(5):892. doi:10.2136/sssaj1980.03615995004400050002x.

85   Balzano B, Tarantino A, Nicotera MV, Forte G, de Falco M, Santo A. Building physically based models for assessing rainfall-induced shallow landslide hazard at catchment scale: case study of the Sorrento Penninsula (Italy). Canadian Geotechnical Journal. 2018;13:1-13

86   Pan L, Wierenga P. Finite element methods for modeling water flow in variably saturated porous media: numerical oscillation and mass-distributed schemes. Water Resources Research. 1996;32(6):1883-1889

87   Mirbagheri Y, Nahvi H, Parvizian J, Duster A. Reducing spurious oscillations in discontinuous wave propagation simulation using higher-order finite elements. Computers and Mathematics with Applications. 2015;70(7):1640-1658

88   Wu S, Qui W. Nonlinear transient dynamic analysis by explicit finite element with iterative consistent mass matrix. Communications in Numerical Methods in Engineering. 2009;25:201-217

89   Wang D, Liu W, Zhang H. Novel higher order mass matrices for isogeometric structural vibration analysis. Computer Methods in Applied Mechanics and Engineering. 2013;260:92-108

90   Scardovelli R, Zaleski S. Direct Numerical Simulation of Free-Surface and Interfacial Flow. Annual Review of Fluid Mechanics. 1999;31(1):567–603. doi:10.1146/annurev.fluid.31.1.567.

91   Manservisi S, Scardovelli R. A variational approach to the contact angle dynamics of spreading droplets. Computers & Fluids. 2009;38:406–424.

92   Young WB. Analysis of capillary flows in non-uniform cross-sectional capillaries. Colloids and Surfaces A: Physicochemical and Engineering Aspects. 2004;234(1–3):123–128. doi:10.1016/j.colsurfa.2003.12.007.

93   Zhu G, Yao J, Zhang L, Sun H, Li A, Shams B. Investigation of the dynamic contact angle using a direct numerical simulation method. Langmuir. 2016;32(45):11736–11744. doi:10.1021/acs.langmuir.6b02543.

94   Blake TD, Haynes JM. Kinetics of liquidliquid displacement. Journal of Colloid and Interface Science. 1969;30(3):421–423. doi:https://doi.org/10.1016/0021-9797(69)90411-1.

95   Cox RG. The dynamics of the spreading of liquids on a solid-surface. Part 1. Viscous-flow. Journal of Fluid Mechanics. 1986;168:169–194. doi:10.1017/S0022112086000332.

96   Blake TD. The physics of moving wetting lines. Journal of Colloid and Interface Science. 2006;299(1):1–13. doi:10.1016/j.jcis.2006.03.051.

97   Jiang T-S, Soo-Gun OH, Slattery JC. Correlation for dynamic contact angle. Journal of Colloid and Interface Science. 1979;69(1):74–77. doi:https://doi.org/10.1016/0021-9797(79)90081-X.

98   Bracke M, De Voeght F, Joos P. The kinetics of wetting: the dynamic contact angle. In: Bothorel P, Dufourc EJ, eds. Trends in Colloid and Interface Science III. Darmstadt: Steinkopff; 1989:142–149.

99   Selvarajoo T, Davies RE, Gardner DR, Freeman BL, Jefferson AD. Characterisation of a vascular self-healing cementitious material system: flow and curing properties. 2019. Submitted for publication

100   Comyn J. Moisture cure of adhesives and sealants. International Journal of Adhesion and Adhesives. 1998;18(4):247–253. doi:10.1016/S0143-7496(97)00031-6.

101   Tomlinson SK, Ghita OR, Hooper RM, Evans KE. The use of near-infrared spectroscopy for the cure monitoring of an ethyl cyanoacrylate adhesive. Vibrational Spectroscopy. 2006;40(1):133–141. doi:10.1016/j.vibspec.2005.07.009.

102   Cambridge Polymer Group. Fourier Transform Infrared Spectroscopy.; 2004.

103   Li YJ, Barthès-Biesel D, Salsac A V. Polymerization kinetics of n-butyl cyanoacrylate glues used for vascular embolization. Journal of the Mechanical Behavior of Biomedical Materials. 2017;69(January):307–317. doi:10.1016/j.jmbbm.2017.01.003.

104   Ogata A, Banks RB. A solution of the differential equation of longitudinal dispersion in porous media. Geological Survey (U.S.).; Professional paper 1961:A1–A7.

105   Metry AA. Predictive tools for contaminant transport in groundwater. ASTM Special Technical Publication 1981:197–208.

106   Jaiswal DK, Kumar A, Yadav RR. Analytical solution to the one-dimensional advection-diffusion equation with temporally dependent coefficients. Journal of Water Resource and Protection. 2011;3(1):76–84. doi:10.4236/jwarp.2011.31009.

107   Bassett B. ∫ e-x2 dx and the Kink Soliton. Computers and Mathematics with Applications. 1998;36(4):37–45. doi:10.1016/S0898-1221(98)00139-4.

108   Reyes MA, Arcos-Olalla R. Supersymmetric features of the error and Dawson's functions. Revista mexicana de fˊısica. 2015;61(6):475-480.

109   Castro JM, Macosko CW. Kinetics and rheology of typical polyurethane reaction injection molding systems. Society of Plastics Engineers (Technical Papers) 1980:434–438.

110   Ivankovic M, Incarnato L, Kenny JM, Nicolais L. Curing kinetics and chemorheology of epoxy/anhydride system. Journal of Applied Polymer Science. 2003;90(11):3012–3019.

111   Teyssandier F, Ivanković M, Love BJ. Modeling the effect of the curing conversion on the dynamic viscosity of epoxy resins cured by an anhydride curing agent. Journal of Applied Polymer Science. 2010;115:1671–1674. doi:10.1002/app.

112   Einstein A. Eine neue bestimmung der molekuldimensionen. Annalen der Physik. 1906;19(2):289–306.

113   Einstein A. Berichtigung zu meiner Arbeit: „Eine neue bestimmung der moleküldimensionen". Annalen der Physik. 1911;339(3):591–592. doi:10.1002/andp.19113390313.

114   Chong JS, Christiansen EB, Baer AD. Rheology of concentrated suspensions. Journal of Applied Polymer Science. 1971;15(8):2007–2021. doi:10.1002/app.1971.070150818.

115   Ghanbari A, Karihaloo BL. Prediction of the plastic viscosity of self-compacting steel fibre reinforced concrete. Cement and Concrete Research. 2009;39(12):1209–1216. doi:10.1016/j.cemconres.2009.08.018.

116   Struble L, Sun GK. Viscosity of Portland cement paste as a function of concentration. Advanced Cement Based Materials. 1995;2(2):62–69. doi:10.1016/1065-7355(95)90026-8.

117   Selvarajoo T, Davies RE, Freeman BL, Jefferson AD. Characterisation of a vascular self-healing cementitious material system: mechanical damage and healing properties. 2019. Submitted for publication

118   Kameche ZA, Ghomari F, Choinska M, Khelidj A. Assessment of liquid water and gas permeabilities of partially saturated ordinary concrete. Construction and Building Materials. 2014;65:551-565

119   Monlouis-Bonnaire JP, Verdier J, Perrin B. Prediction of the relative permeability to gas flow of cement-based materials. Cement and Concrete Research. 2004;34(5):737-744

120   Poyet S, Charles S, Honoré N, L'Hostis V. Assessment of the unsaturated water transport properties of an old concrete: determination of the pore-interaction factor. Cement and Concrete Research. 2011;41(10):1015-1023

121   Karihaloo BL. Fracture mechanics and structural concrete. Longman Scientific & Technical, New York, 1995